## Chapter 3

# Physics Studies with Muons

## 3.1 Benchmark Channel: $H \to ZZ^{(*)} \to 4$ muons

The $\mathrm{H} \to \mathrm{ZZ}^{(*)} \to 4\mu$ process is one of the cleanest channels for discovering the Standard Model Higgs boson at LHC. This section presents the CMS potential for discovering the Higgs boson in this decay mode and measuring its mass, width, and production cross section, in the range of Higgs boson masses from 115 GeV/c$^2$ to 600 GeV/c$^2$. Both signal and background event samples are generated at the Leading Order (LO) approximation, and Next to Leading Order (NLO) production cross sections, computed using different methods, are used for their normalisation. To simulate the detector response and reconstruct physics objects, the full CMS detector simulation and reconstruction software was used. A full treatment of the most important theoretical and instrumental systematic uncertainties are presented, together with their effect on the evaluation of the significance of the Higgs boson observation and on the measurement of its parameters. To minimise systematic uncertainties, new methods of reconstructing the most important corrections directly from data were developed.

### 3.1.1 Physics processes and their simulation

The Higgs boson event samples for 18 Higgs boson mass points and the three main background processes, $t\bar{t}$, $(\mathrm{Z}^{(*)}/\gamma^*)\mathrm{b\bar{b}}$ and $(\mathrm{Z}^{(*)}/\gamma^*)(\mathrm{Z}^{(*)}/\gamma^*)$ were simulated using the CMS simulation [8] and reconstruction [10] software. These three backgrounds will be hereafter referred to as $t\bar{t}$, $\mathrm{Zb\bar{b}}$ and ZZ, respectively. Details on the generator-level simulation conditions, cross sections and K-factors can be found in [51]. Many other plausible background candidates, $\mathrm{b\bar{b}b\bar{b}}$, $\mathrm{b\bar{b}c\bar{c}}$, $\mathrm{c\bar{c}c\bar{c}}$, single-top, $\mathrm{Zc\bar{c}}$, $\mathrm{Wb\bar{b}}$, $\mathrm{Wc\bar{c}}$, fake and $\pi/\mathrm{K}$ decay muons in QCD, were considered and found to be negligible.

Only events with at least $2\mu^+$ and $2\mu^-$ in pseudorapidity range $|\eta| < 2.4$ and with $p_T > 3$ GeV/c were retained for further analysis. Muons outside these kinematic limits could not be reconstructed in the CMS detector. Additional cuts were applied on dimuon invariant masses for the Higgs boson samples ($m_{\mathrm{Z}} > 5$ GeV/c$^2$) and for ZZ and $\mathrm{Zb\bar{b}}$ samples ($m_{\mu^+\mu^-} > 5$ GeV/c$^2$). The first $\mu^+\mu^-$ pair in the ZZ and $\mathrm{Zb\bar{b}}$ samples was defined as the one with its invariant mass closest to $m_{\mathrm{Z}}$, while the second $\mu^+\mu^-$ pair was made out of the two remaining highest $p_T$ muons of opposite charge. These cuts do not bias the Monte Carlo samples since all the analysis cuts, described below, are tighter.

The Higgs boson samples were generated with PYTHIA 6.225 [24] (LO gluon and weak boson fusion, $\mathrm{gg} \to \mathrm{H}$ and $\mathrm{q\bar{q}} \to \mathrm{q\bar{q}H}$) interfaced via CMKIN [52]. Events were re-weighted to correspond to the total NLO cross section $\sigma(\mathrm{pp} \to \mathrm{H}) \cdot BR(\mathrm{H} \to \mathrm{ZZ}) \cdot BR(\mathrm{Z} \to 2\ell)^2$ (Fig. 3.1).

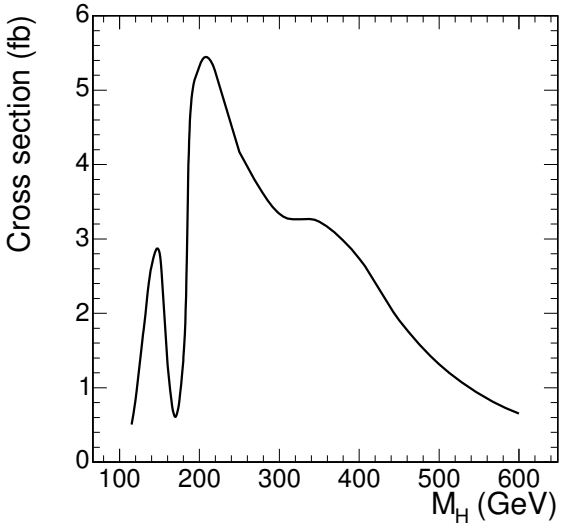


Figure 3.1: Standard Model NLO cross section for the process $\mathrm{H} \to \mathrm{ZZ}^{(*)} \to 4\mu$ *vs.* Higs boson mass.

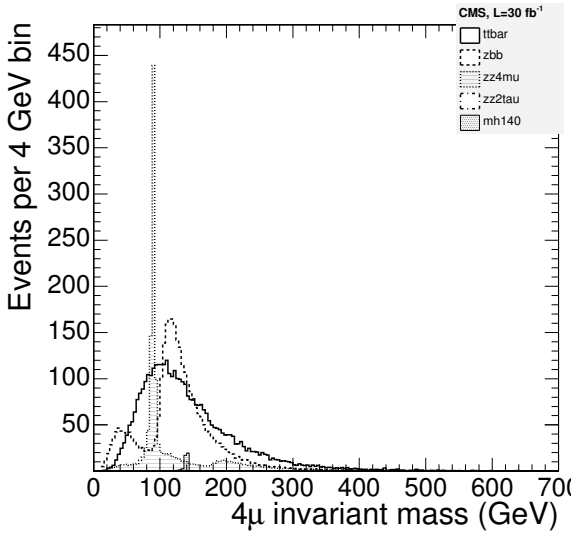


Figure 3.2: Distributions of $\mathrm{m}_{4\mu}$ after pre-selection cuts for $t\bar{t}$, $\mathrm{Zb\bar{b}}$, ZZ and a Higgs boson signal of $m_{\mathrm{H}} = 140\,\mathrm{GeV/c^2}$.

The cross section $\sigma(\mathrm{pp} \to \mathrm{H})$ and the branching ratio $BR(\mathrm{H} \to \mathrm{ZZ})$ were taken from [53]; $BR(\mathrm{Z} \to 2\ell) = 0.101$ [54]. Interference of permutations of identical leptons originating from different Z bosons results in an enhancement to the cross section for $\mathrm{H} \to \mathrm{ZZ}^{(*)} \to 4\ell$ processes with identical leptons [51], which is about 15% for $m_{\mathrm{H}} = 115\,\mathrm{GeV/c^2}$ and steadily goes to zero for $m_{\mathrm{H}} = 180\,\mathrm{GeV/c^2}$. This correction was calculated with COMPHEP.

The $t\bar{t}$ sample was generated with PYTHIA 6.225 (LO $\mathrm{gg} \to \mathrm{t\bar{t}}$ and $\mathrm{q\bar{q}} \to \mathrm{t\bar{t}}$). Events were re-weighted to correspond to the total NLO cross section $\sigma(\mathrm{pp} \to \mathrm{t\bar{t}}) \cdot BR(\mathrm{W} \to \ell\nu)^2$. The NLO cross section $\sigma(\mathrm{pp} \to \mathrm{t\bar{t}}) = 840$ pb was taken from [55] and the branching ratio $BR(\mathrm{W} \to \ell\nu) = 0.320$ from [54].

The $\mathrm{Zb\bar{b}} \to \mu^+\mu^-\mathrm{b\bar{b}}$ sample was generated with the COMPHEP 4.2p1 [43] matrix element generator, interfaced to PYTHIA 6.225 for showering and hadronisation. Included sub-processes were $\mathrm{q\bar{q}/gg} \to (\mathrm{Z}/\gamma^*)\mathrm{b\bar{b}} \to \mu^+\mu^-\mathrm{b\bar{b}}$. The corresponding COMPHEP LO cross section was found to be 116 pb. To obtain the NLO cross section a NLO K-factor $K_{NLO} = 2.4 \pm 0.3$, computed with MCFM [56], was used.

The $\mathrm{q\bar{q}} \to \mathrm{ZZ} \to 4\mu$ and $\mathrm{q\bar{q}} \to \mathrm{ZZ} \to 2\mu 2\tau$ event samples were generated with COMPHEP, including both the t- and s-channel diagrams [57]. The COMPHEP events were further interfaced to PYTHIA 6.225 for showering and hadronisation. The COMPHEP LO cross sections for the two sub-processes were 113 fb and 157 fb. To account for contributions due to all the NLO diagrams and due to the NNLO gluon fusion ($\mathrm{gg} \to \mathrm{ZZ}$, known to contribute $\sim 20\%$ with respect to the LO [42] cross section), events are reweighted with the $\mathrm{m}_{4\mu}$-dependent K-factor $K(\mathrm{m}_{4\mu}) = K_{NLO}(\mathrm{m}_{4\mu}) + 0.2$. The NLO K-factor $K_{NLO}(\mathrm{m}_{4\mu})$ was obtained with MCFM. The details on the dynamic differences between NLO and LO are summarised elsewhere [58].

The $\mathrm{m}_{4\mu}$ distributions for a Higgs boson signal of $m_{\mathrm{H}} = 140\,\mathrm{GeV/c^2}$ and the main backgrounds are shown in Fig. 3.2 after the pre-selection cuts described above.

### 3.1.2 Event selection

#### 3.1.2.1 Trigger and offline muon selection

CMS has been designed and optimised to detect and reconstruct muons. These particles provide a very clean signature and thus a very high trigger efficiency, with an average of 98% for the Level-1 Global Muon Trigger [7]. The inclusive muon triggers based on the selection of a single muon with $p_T > 19\,\text{GeV/c}$ or dimuons with $p_T > 7\,\text{GeV/c}$ assures an efficiency of practically 100% for collecting events with four high-$p_T$ muons.

In order to minimise muon reconstruction systematic uncertainties, we select only those reconstructed muons that have transverse momentum $p_T > 7\,\text{GeV/c}$, if they are in the central pseudo-rapidity region ($|\eta| < 1.1$), or with momentum $p > 13\,\text{GeV/c}$, if they are in the end-caps ($|\eta| > 1.1$) [59]. These cuts do not affect the number of accepted signal events significantly.

Also, we require that all four possible combinations of the reconstructed dimuon masses be above $12\,\text{GeV/c}^2$, $m_{\mu^+\mu^-} > 12\,\text{GeV/c}^2$. As in the previous case, this cut has a very little effect on the Higgs boson events and is primarily intended to suppress poorly simulated hadron background contributions originating from charmonium and bottomium dimuon decays.

#### 3.1.2.2 Discriminating variables

The $\mathrm{H} \to \mathrm{ZZ}^{(*)} \to 4\mu$ signal presents a characteristic topology, which consists of two opposite charge muon-pairs in the final state. All four muons are isolated, have a high transverse momentum and point to the same Z-boson mass, depending on the restrictions in the phase space introduced by the Higgs boson mass itself. The four-muon invariant mass peaks at the Higgs boson mass, within the detector resolution. The width of the resonant peak accounts for the natural Higgs boson width and the detector resolution.

In $\mathrm{Zb\bar{b}}$ and $t\bar{t}$ background events, two of the muons come from b-quark decays and are usually found within a jet (i.e., non-isolated), have lower transverse momenta and often exhibit detectable displaced vertices. The isolation is defined as the amount of transverse energy in the calorimeter (calorimeter isolation), or the sum of the transverse momentum of the tracks reconstructed in the tracker (tracker isolation), inside a cone in $\eta$-$\phi$ space with a radius $R \equiv \sqrt{(\Delta\eta)^2 + (\Delta\phi)^2}$ around each muon. Figure 3.3 (left) shows the distribution of the calorimeter isolation variable for the least isolated muon, for two potential Higgs boson signals, $150\,\text{GeV/c}^2$ and $300\,\text{GeV/c}^2$, and for the background. Requiring a maximum isolation in all four muons drastically suppresses $t\bar{t}$ and $\mathrm{Zb\bar{b}}$ contamination.

Further restrictions on the $p_T$ spectrum of the 2 lowest $p_T$ muons in the event (see Figure 3.3 (right), for the 2nd lowest $p_T$ muon) reduces even more the $t\bar{t}$ and $\mathrm{Zb\bar{b}}$ contamination. In this way, the ZZ background, which presents a topology very similar to that of the signal, becomes the dominant and irreducible background. Only the four-muon mass distribution, the main discriminant, allows the resonant Higgs signal to be identified over the continuum ZZ production.

Distinction on the basis of dimuon invariant mass or displaced vertices does not increase the Higgs boson signal over the ZZ background. However, they may play an important role in eliminating other possible unaccounted for backgrounds, arising from the primary interactions, accelerator beam halo, detector mis-performance, etc.

Additional variables that may help discriminating H from the dominant ZZ background

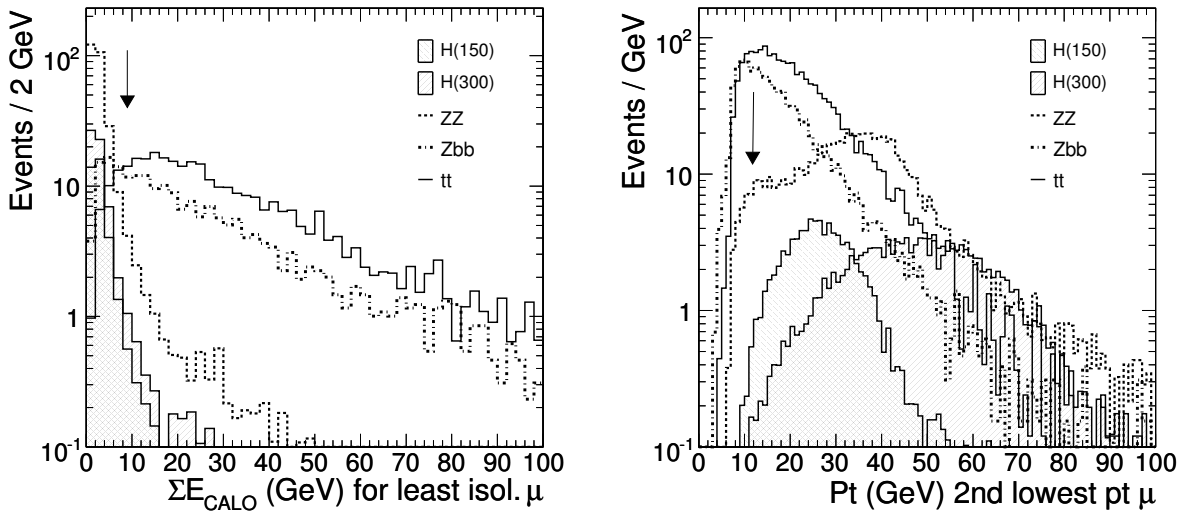


Figure 3.3: Examples of discriminating variables: (left) muon calorimeter-based isolation $\sum E_T$ for the least isolated muon and (right) transverse momentum of the $2^{\text{nd}}$ lowest $p_T$ muon. The hatched histograms represent the Higgs boson signals of masses 150 GeV/c$^2$ and 300 GeV/c$^2$, while the solid, dashed and dash-dotted lines indicate the contribution from the $t\bar{t}$, ZZ and $\mathrm{Zb\bar{b}}$ backgrounds, respectively. The arrows indicate the positions of the cuts.

have been studied: $p_T(4\mu)$, number of jets and their $E_T$, etc. However, these variables are driven by the NLO production processes, while our samples were generated at the Leading Order by PYTHIA and COMPHEP. Therefore, any conclusions that we might derive from these samples would not be reliable. Some muon angular distributions also have some differences originating from the underlying spin structures, but they are not sufficiently discriminating to be used and may be strongly affected by the NLO diagrams.

### 3.1.3 Higgs boson search analysis

#### 3.1.3.1 Search using $\mathrm{m}_{4\mu}$-independent cuts

Given the clear signature of the Higgs boson events, the signal extraction has been performed with a unique set of cuts, independent the Higgs boson mass, the details can be found in [51]. A Higgs mass-independent analysis is expected to minimise the dependence on the simulation of the discriminating variables in the Monte Carlo and the sensitivity to systematic errors. It is also readily applicable to real data and robust under variations of the detector conditions (calibrations, resolutions, efficiencies). Moreover, in our case, a mass-dependent selection does not significantly increase the significance of observing a signal.

A unique set of selection cuts has been designed to make the analysis robust when applied to real data. As explained below, some of the cuts (dimuon invariant mass, $p_{\mathrm{T}}$ cuts on the two hardest muons and isolation cuts on the two most isolated muons) slightly decrease the signal significance but make the selection more robust under imperfect conditions in the detector.

A loose requirement on the invariant mass of the pair of unlike-sign muons in the event which is closer to the nominal Z-boson mass, namely, $70\,\text{GeV/c}^2 < m_{\mu^+\mu^-} < 100\,\text{GeV/c}^2$, leaves more than 90% of the signal, while eliminating around 50% of the $t\bar{t}$ contamination.

The loss in the signal is due to the internal bremsstrahlung and $Z \to 2\tau \to 2\mu 4\nu$ decays.

Cuts of 12 GeV/c and 8 GeV/c are set on the $p_T$ of the two lowest-$p_T$ muons. The $p_T$ of the two highest-$p_T$ muons must be larger than 15 GeV/c. The latter cut affects neither the signal nor the background, but is considered useful for eliminating unexpected background in real data. The efficiency of the $p_T$ cuts in the signal is close to 90% while it suppresses around 50% of the remaining $Zb\bar{b}$ events, 40% of the $t\bar{t}$ events and about 20% of the ZZ background.

For the purposes of the isolation cut optimisation, different cone radii and several energy and transverse momentum thresholds have been studied. Those yielding the maximum signal significance are, for calorimeter isolation, a cone radius of 0.24 and energy thresholds of 5 GeV and 9 GeV, while for tracker isolation a cone radius of 0.20 and $p_T$ thresholds of 2.5 GeV/c and 4 GeV/c. The numbers are given for the two least isolated muons. Although a requirement on the isolation of the two most isolated muons does not increase the signal significance, following the same argument as in the case of the $p_T$ cuts, a cut of 3.5 GeV/c and 5 GeV/c for the calorimeter isolation and 2 GeV/c and 2.5 GeV/c for the tracker isolation is set for the two most isolated muons.

After these cuts, $Zb\bar{b}$ and $t\bar{t}$ events are suppressed to a negligible level in comparison to the remaining ZZ background. The efficiencies of each selection cut over the signal, for the 18 Higgs mass points studied, are shown in Figure 3.4 (left). The four-muon mass distributions for signal and background events that survive the selection cuts are displayed in Figure 3.4 (right).

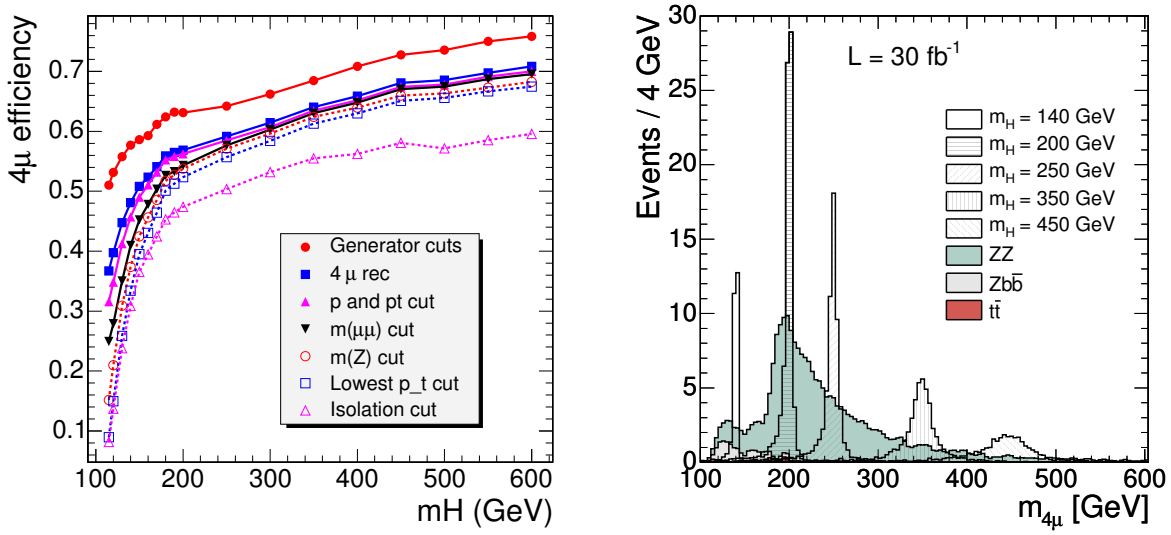


Figure 3.4: (Left) $H \to ZZ^{(*)} \to 4\mu$ efficiency *vs.* $m_H$ after different cuts are applied. (Right) Reconstructed four-muon invariant mass distribution, for an integrated luminosity of 30 $fb^{-1}$, for background (shaded histograms) and several Higgs signals (hatched), after the selection criteria are applied.

In order to estimate the statistical significance of the signal, the log-likelihood ratio (LLR) statistical method [60, 61] is used. The distribution to discriminate signal and background is the four-muon invariant mass (Fig. 3.4 (right)). This distribution, for each Higgs boson mass hypothesis and for the background, is used to calculate the log likelihood ratio, $-2 \ln Q$, which is then used to evaluate the compatibility of the data with either the *signal plus background* or

the *background-only* hypothesis [51]. The $-2\ln Q$ estimator is sensitive both to the normalisation and the shape of the discriminant. Each event in the sum has a weight $\ln(1+s/b)$ which depends on the signal-to-background ratio, $s/b$, in the bin where it is found, which in turn depends on the $m_{\mathrm{H}}$ hypothesis. The whole spectrum of the discriminant variable enters the LLR calculation. This avoids any ambiguity in the definition of a signal region for determining the signal significance, present in counting methods.

Figure 3.5 (left) shows the statistical significance, $S_L \equiv \sqrt{<2\ln Q>}$, for an integrated luminosity 30 fb$^{-1}$ at different $\mathrm{m}_{4\mu}$ invariant masses, should the Higgs boson exist at one of these masses. Based on this distribution, the plot on the right depicts the integrated luminosity required to reach a statistical significance of the signal of $3\sigma$ and $5\sigma$, as function of $m_{\mathrm{H}}$. The expected integrated luminosity required to exclude the signal at the 95% confidence level in a background-only experiment is also shown as function of $m_{\mathrm{H}}$. The effect of including systematic uncertainties (subsection 3.1.3.3) in the calculation of $S_L$ is at the level of 15%-20% of the statistical accuracy of the expected significance, supporting that this analysis is not dominated by systematic uncertainties.

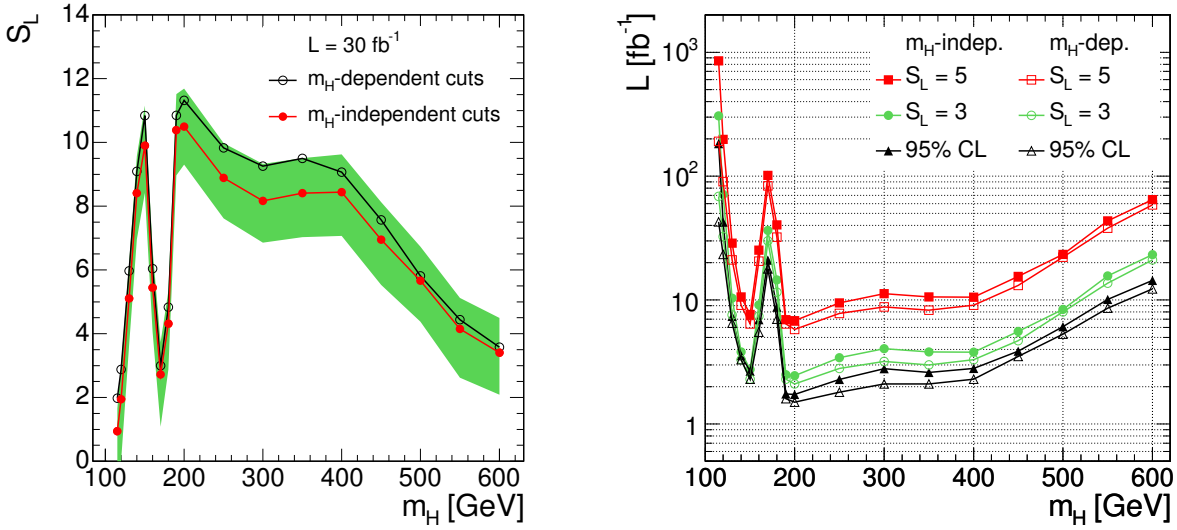


Figure 3.5: (Left) Statistical significance of the signal, $S_L$, as function of the Higgs boson mass for an integrated luminosity of 30 fb$^{-1}$, for mass-independent cuts (filled circles) and mass-dependent cuts (empty circles). The shaded band represents the statistical uncertainty on $S_L$. (Right) Integrated luminosity, for mass-independent (lines with filled squares, circles, and triangles) and mass-dependent cuts (lines with empty pointers), required to achieve a statistical significance of three (middle pair of curves) and five (upper pair of curves) standard deviations, as a function of the Higgs mass. The integrated luminosity required for excluding a Higgs boson signal at the 95% C.L. in a background-only experiment is also displayed (lower pair of curves).

In order to more accurately quantify the degree of compatibility of the observed data with any of the two hypotheses, the confidence levels $\mathrm{CL}_b$ and $\mathrm{CL}_s$ are defined using the $-2\ln Q$ probability density functions, pdf, for both the background-only and the signal-plus-background hypotheses (details can be found in Refs. [51, 60]).

The presence of a signal can be inferred from the behaviour of $1-\mathrm{CL}_b$ for the background-only hypothesis, which is the probability of observing in a sample of simulated background-

only experiments a more signal-like value of $-2 \ln Q$. The observation of the value $1-\mathrm{CL}_b = 2.85 \times 10^{-7}$ indicates a $5\sigma$ excess in the data with respect to the background expectation. While $\mathrm{CL}_b$ quantifies the lack of compatibility of an excess of observed events with the background-only hypothesis, $\mathrm{CL}_s$ gives information about how compatible it is with an actual signal (Fig. 3.6).

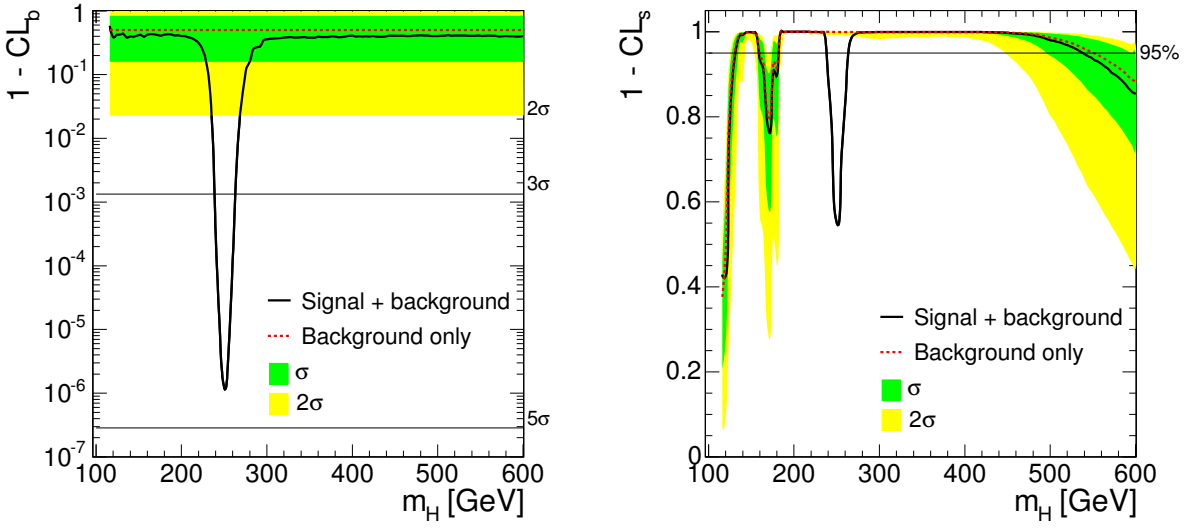


Figure 3.6: Mean values for $1 - \mathrm{CL}_b$ (left) and $1 - \mathrm{CL}_s$ (right) as a function of the Higgs boson mass hypothesis, assuming existence of Higgs boson at 250 GeV/c$^2$ mass and for an integrated luminosity of 10 fb$^{-1}$. The observation of the Higgs is just a little be shy of the $5\sigma$ discovery (left). The mass points for which the curve $1 - \mathrm{CL}_s$ is above 0.95 are excluded at 95% CL (right). The $1\sigma$ and $2\sigma$ bands on $1 - \mathrm{CL}_b$ and $1 - \mathrm{CL}_s$, originating from the Poisson statistical fluctuations of the number of background events in each bin of the discriminant distribution, are also shown.

#### 3.1.3.2 Search using $\mathrm{m}_{4\mu}$-dependent cuts

One can take advantage of the fact that the Higgs boson resonance $\mathrm{H} \to \mathrm{ZZ}^{(*)} \to 4\mu$ is relatively narrow and use $\mathrm{m}_{4\mu}$-dependent cuts for its search. All details of such search strategy can be found in [51]. The analysis steps in this case would be as follows:

- First, events with 4 muons ($2\mu^+2\mu^-$) satisfying $p_T$, $p$, and $m_{\mu^+\mu^-}$ quality cuts as described in section 3.1.2.1 are selected. This ensures that muons are reliably reconstructed and removes a "contamination" originating from heavy quarkonia decays.
- Second, after reconstructing a four-muon invariant mass, the $\mathrm{m}_{4\mu}$-dependent cuts are applied. The cuts, being smooth functions of $\mathrm{m}_{4\mu}$, are optimised in such a way that they maximise the significance of the Higgs signal excess *at all Higgs boson mass points*.
- And finally, the resulting $\mathrm{m}_{4\mu}$ distribution is analysed for the presence of a Higgs boson resonance. The search can be done using either the LLR significance $S_L$ estimator built for the whole spectrum or the LLR $S_{cL}$ estimator built for a single-bin, or signal window (counting experiment). The direct comparison of the results can be found in [51].

To perform the desired $\mathrm{m}_{4\mu}$-dependent cut optimisation, we used a recently developed program GARCON [62]. The counting experiment significance estimator $S_{cL}$ is the natural tool for such optimisation. The first half of the available Monte Carlo statistics was used for the cut optimisation. The results for the 18 Higgs mass points were then fit to obtain smooth $\mathrm{m}_{4\mu}$-dependent cuts. It was found that, given the level of the expected dominant backgrounds ($t\bar{t}$, $\mathrm{Zb\bar{b}}$, ZZ), there are only three critical discriminating cuts (details are given in Ref. [51]):

- The muon isolation cut, both tracker- and calorimeter-based, on the worst isolated muon, or equivalently one common cut on all four muons. This cut strongly suppresses $t\bar{t}$ and $\mathrm{Zb\bar{b}}$ backgrounds. The cuts gets tighter and tighter as $\mathrm{m}_{4\mu}$ gets smaller since $\mathrm{Zb\bar{b}}$ and $t\bar{t}$ increase (Fig. 3.2).
- The $p_T$ on the second lowest $p_T$ muon, or equivalently one common cut on the three highest $p_T$ muons. This cut helps to further suppress $\mathrm{Zb\bar{b}}$ background to the level well below ZZ and reduces the ZZ background at high four-muon invariant masses. This cut becomes more stringent with increasing $\mathrm{m}_{4\mu}$.
- The $\mathrm{m}_{4\mu}$ window being used for scanning over the background. It roughly corresponds to the $\pm 2\sigma$ width, where $\sigma$ is the Higgs boson peak width that includes the detector resolution and the Standard Model Higgs boson width.

The final results are obtained by applying these cuts to the second half of the available Monte Carlo statistics. The observed stability of the results ensures that the cut optimisation did not pick peculiar phase space corners corresponding to statistical flukes. After applying the cuts, the $t\bar{t}$ and $\mathrm{Zb\bar{b}}$ backgrounds are now suppressed well below the irreducible ZZ background.

Figure 3.5 shows, for different Higgs boson masses, the expected significance $S_L$ at $\mathcal{L} = 30\,\mathrm{fb}^{-1}$ (left) and the average integrated luminosities at which a "$5\sigma$-discovery", "$3\sigma$-evidence", and exclusion at 95%CL are expected (right). The gain in significance with respect to the flat, $\mathrm{m}_{4\mu}$-independent, cuts can be easily translated into probabilistic terms. For example, the Higgs boson with $m_{\mathrm{H}} = 130\,\mathrm{GeV/c^2}$ is right at the "$5\sigma$-discovery" threshold for an integrated luminosity $\mathcal{L} = 30\,\mathrm{fb}^{-1}$. The difference in the average expected significance, 5.1 and 6.0, means in this case that the chances of observing significance in excess of 5 for $m_{\mathrm{H}} = 130\,\mathrm{GeV/c^2}$ at $\mathcal{L} = 30\,\mathrm{fb}^{-1}$ are $55\%$ for the flat cuts and $80\%$ for the $\mathrm{m}_{4\mu}$-dependent cuts.

#### 3.1.3.3 Systematic errors

The analysis of the systematic errors can be sub-divided into two distinct stages. First, one needs to understand the level of uncertainties in predicting the level of background in the vicinity of a particular $\mathrm{m}_{4\mu}$ point being investigated for a possible event excess. Second, these uncertainties in the background need to be included in the evaluation of the significance of an excess of events, should it be observed.

Uncertainties in the signal are not very important for establishing an excess of events over the background. It is the uncertainties in the background that are of main concern. After applying the analysis cuts as described earlier, the ZZ production is the dominant irreducible background with all other processes giving much smaller contributions. This reduces the analysis of systematic errors to those of the $\mathrm{ZZ} \to 4\mu$ process.

One can try to evaluate the theoretical and detector performance related uncertainties starting from the first principles. However, especially during the earlier stages of the detector operation when the changes in the system are frequent and hard to monitor and timely

incorporate into the detector Monte Carlo simulation, these estimations have limited predictability. Therefore, we developed methods evaluating various corrections, such as muon reconstruction efficiency, muon isolation cut efficiency, directly from data in order to minimise reliance on the Monte Carlo simulation, and, thus, significantly reducing the associated systematic errors. Also, throughout this analysis, we estimate the background around a particular $\mathrm{m}_{4\mu}$ with reference to a *measured* control sample. Note that this completely eliminates uncertainties associated with measuring the luminosity and reduces the sensitivity to PDF and QCD-scales. For the control sample, we use either the inclusive $\mathrm{Z} \to 2\mu$ process or sidebands of the $\mathrm{m}_{4\mu}$ spectrum itself.

The main uncertainties can be grouped as follows:

1. Uncertainties associated with the background production rates, *i.e.* not directly related to CMS Detector performance itself:
   - ZZ: PDF and QCD scale uncertainties described in details in Ref. [47].
   - ZZ: NLO and NNLO contributions vs LO described in details in Ref. [58] plus some related issues are discussed in Ref. [42]. These possible uncertainties are not taken into account in the results shown below, for details see Ref. [51].
   - LHC luminosity: when we estimate the ZZ background events in the signal region via the measured number of events in the control samples, the luminosity uncertainties largely cancel out.

2. Uncertainties associated with the CMS detector performance (hardware/software) and our analysis-specific cuts:
   - ZZ: Trigger efficiency, being very close to 100% due to presence of four muons, does not have substantial systematic errors.
   - ZZ: The muon reconstruction efficiency is determined directly from data [59]. The associated systematic error is less than 1% per muon. Using normalisation to the measured $\mathrm{Z} \to 2\mu$ process, this leaves us with 2% uncertainty per event for the $\mathrm{ZZ} \to 4\mu$ background production.
   - ZZ: The muon isolation cut efficiency is also determined directly from data [63] with about 2% uncertainty per event.
   - Higgs: $\mathrm{m}_{4\mu}$ resolution is affected by muon $p_T$ resolution. This almost does not affect the background distribution. In [51], we show that even making a mistake in the $\mathrm{m}_{4\mu}$ distribution width by as much as 25% has only a tiny effect on evaluating a significance of an excess of events. The muon $p_T$ resolution is fairly easy to measure from data using the measured $J/\psi$ and $Z$ peak widths with the precision much better than needed.
   - ZZ: $\mathrm{m}_{4\mu}$ scale. The effect of these uncertainties on the number of background events in a signal window appears only on steep slopes of the $\mathrm{m}_{4\mu}$ distribution. For the steepest part of the $\mathrm{m}_{4\mu}$ distribution in the 180 GeV/c$^2$-200 GeV/c$^2$ range, we obtain $\delta b/b \sim 0.1\,\delta \mathrm{m}_{4\mu}$, where $\mathrm{m}_{4\mu}$ is in GeV/c$^2$ and $b$ is the number of background events. This implies that to be able to neglect this effect, one needs to know the momentum scale with precision of $0.1$ GeV at $p_T \sim 50$ GeV/c. This can be easily achieved with just a few hundreds of $\mathrm{Z} \to 2\mu$ events.

Fig. 3.7 summaries all systematic errors on the expected number of events in the $Z \rightarrow 4\mu$ background for the two methods: via referencing to the total measured $Z \rightarrow 2\mu$ cross section and via referencing to the event count in the sidebands of the $m_{4\mu}$ spectrum itself.

**Significance with the background uncertainties included:**

For the Gaussian-like signal over relatively flat background, the $S_L$ and $S_{cL}$ estimators are strongly correlated, with the typical difference of 5%-10% [51]. This stems from the fact that the signal peak is very localised and the background is relatively flat. This allows us to study the effect of systematic errors on the evaluation of significance at the time of measurements using the counting experiment approach, for which everything can be done analytically. All details on the method we use can be found in Ref. [51]. The method allows to account for the theoretical and instrumental systematic errors as well as for statistical errors when a control sample with a limited event count is used.

The final result of these studies is presented in Figure 3.8. Starting from an integrated luminosity at which the statistical significance of a Higgs boson observation would be equal to 5 (if the level of background without any errors was known), the figure shows how this significance must be de-rated due to the systematic errors at the time of the measurements as described in the previous sub-section. The effect of systematic errors at low or high luminosities is not as important: at lower luminosity the significance is not sufficient to make serious claims, anyway; while after surpassing the significance of 5, the existence of the Higgs boson can be considered established and the focus must be switched to measuring its parameters.

The two curves with full and open circles show the difference of the two methods for evaluating the background in the signal region: via normalisation to the measured $Z \rightarrow 2\mu$ cross section, and via normalisation to the event count in sidebands ($100\,\mathrm{GeV/c^2}$ to $700\,\mathrm{GeV/c^2}$, excluding the signal region). The effect of systematic errors at lower luminosities becomes smaller for the former method and quickly diverges for the latter. As the luminosity increases, the trends obviously reverse. Around the threshold of $S = 5$, the difference between the two methods is not very dramatic; the true benefit of using two approaches to estimating background from data is in their complementarity.

**Local significance and overall statistical fluctuation probability:**

In a search for a relatively narrow $4\mu$ invariant mass peak over a broad background spectrum, one must take into account that the probability of observing a background fluctuation giving an excess of events consistent with a Higgs hypothesis of *some particular mass* might be considerably higher that the local significance calculated for a given mass might imply. This over-estimation of significance strongly depends on how the analysis is set and what constraints/priors on the "phase space" of parameters are used. *E.g.*, in a search specifically tailored for the Standard Model Higgs, the only free parameter is the Higgs boson mass; its width, production cross section, and decay branching ratios are dependent on the mass. To make the search even more constrained, one can use a prior on the Higgs mass as it comes out from the precision electroweak measurements. A specific case study showing the potential scope of the effect, which may be comparable or even larger than the effect of the systematic errors discussed above, is given in Appendix A.

### 3.1.4 Measurement of the Higgs boson properties at $\mathcal{L} = 30\,\mathrm{fb}^{-1}$

The capabilities of the CMS detector to measure the mass, cross section and width of the Higgs boson are determined for an integrated luminosity of $30\,\mathrm{fb}^{-1}$ [64]. These parameters

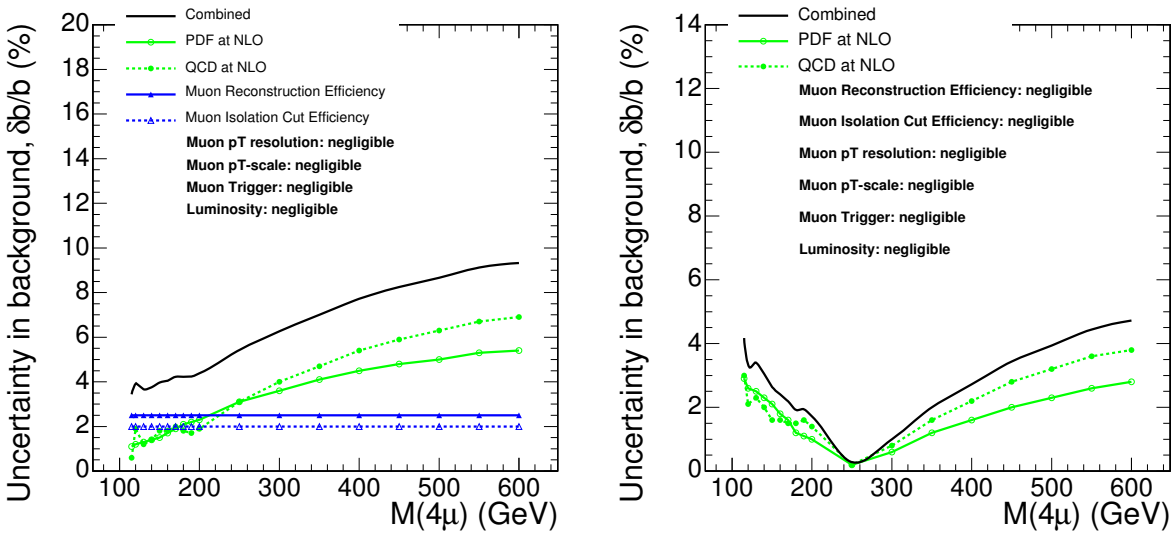


Figure 3.7: Uncertainties in the count of the ZZ $\to 4\mu$ background events in the signal region window at different $\mathrm{m}_{4\mu}$. The window size is $\pm 2\sigma$ of the expected experimental Higgs resonance width. (Left) The background event count in the signal region is derived from the measured number of Z $\to 2\mu$ events. (Right) The background event count in the signal region, $b$, is calculated from the number of ZZ $\to 4\mu$ events $B$ in the range 100 GeV/c$^2$-700 GeV/c$^2$ (excluding the signal region window), i.e. $b = \rho \cdot B$.

are measured using a binned maximum likelihood fit to the reconstructed four-muon invariant mass, which includes the signal and background contributions after all the selection cuts have been applied (Figure 3.4 (right)). The 'observed' distribution, $f_{sb}$, is expressed in terms of the signal, $p_s$, and background, $p_b$, probability density functions (pdf) as:

$$f_{sb}(\mathrm{m}_{4\mu}; m_{fit}, \Gamma, N_s, N_b) = N_s \cdot p_s(\mathrm{m}_{4\mu}; m_{fit}, \Gamma) + N_b \cdot p_b(\mathrm{m}_{4\mu})$$

$N_s$ is the number of signal events, $N_b$ the number of background events, $m_{fit}$ the position of the mass peak and $\Gamma$ the intrinsic width of the Higgs boson. The signal pdf is the sum of two contributions: a convolution of a Breit-Wigner signal shape with a Gaussian distribution that accounts for detector resolution, $p_{core}$, and a function that reproduces the radiative tail due to internal bremsstrahlung, $p_{tail}$:

$$p_s = \beta \cdot p_{core}(\mathrm{m}_{4\mu}; m_{fit}, \Gamma, \sigma) + (1-\beta) \cdot p_{tail}(\mathrm{m}_{4\mu}; m_{fit}, \tau)$$

where $1-\beta$ is the fraction of signal events in the radiative tail. The tail shape is parameterised *ad hoc* as

$$p_{tail} = \frac{(\mathrm{m}_{4\mu} - m_{fit})^2}{2\tau^3} \exp\left(\frac{\mathrm{m}_{4\mu} - m_{fit}}{\tau}\right)$$

if $\mathrm{m}_{4\mu} < m_{fit}$ and is zero otherwise [65]. Figure 3.9 (left) illustrates the different contributions to $f_{sb}$. The $p_s$ function is fitted to the signal-only distributions to obtain the parameters of the radiative tail, which remain fixed in the fit to the signal plus background spectra.

For Higgs boson masses below 190 GeV/c$^2$, the intrinsic width is negligibly small compared to the mass spread introduced by the experimental resolution and the signal is thus approximated by a Gaussian shape. For masses above 400 GeV/c$^2$, the natural width of the Higgs

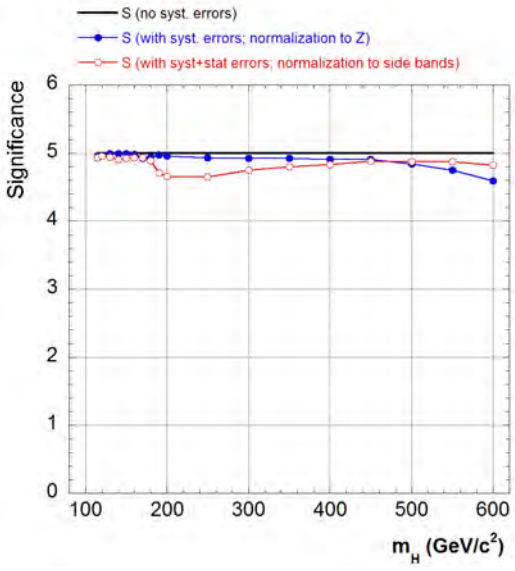


Figure 3.8: Effect of including systematic errors into evaluation of significance at the time of measurements. The reference luminosities, dependent on the Higgs boson mass, are chosen to correspond to an observation of significance $S = 5$ without systematic errors. Solid circles show degrading of significance for the case of systematic errors when the background is evaluated from the measured $Z \to 2\mu$ cross section. Open circles show the effect for the case when the background in signal region is normalised to the sidebands.

is much larger than the experimental resolution, hence the description using a pure Breit-Wigner function yields similar parameters as those obtained from the convolution.

The detector resolution is extracted from the $\mathrm{m}_{4\mu}$ distribution of ZZ events with a four-muon mass above $2m_{\mathrm{Z}}$, for which the kinematics is similar to that of the signal. For masses below $2m_{\mathrm{Z}}$, the intrinsic Higgs boson width is negligible, therefore the resolution is measured directly from the width of the $\mathrm{m}_{4\mu}$ distribution. This width has been found to be consistent with the extrapolation of the resolution determined using ZZ events.

The background pdf, $p_b$, is approximated by either a polynomial or an exponential function, depending on the mass region under study. The parameters are determined performing a binned maximum likelihood fit to the background sample. The parameters defining the shape of the background are fixed in the global fit to signal plus background, but not its normalisation.

The values of the parameters, together with their errors, are obtained directly from the fit. The result of the fit to the signal plus background distribution is shown in Figure 3.9 (right) for a Higgs boson signal of $m_{\mathrm{H}} = 250\,\mathrm{GeV/c^2}$. Figure 3.10 (left) depicts the relative shift of the fitted Higgs boson mass with respect to the true mass, together with its statistical error. These values are compatible with zero in the full range of masses, which means that the true mass is accurately recovered after applying the fitting method to the reconstructed sample. The evolution of the relative error as a function of the true mass is displayed in Figure 3.10 (right), showing that the mass can be measured with precisions from 0.1% to 5.4%. The increase in this error around $170\,\mathrm{GeV/c^2}$ is due to the smaller signal statistics caused by the suppression of the $\mathrm{H} \to \mathrm{ZZ}^{(*)}$ decay at this mass. The increasing uncertainty at higher masses is due to the smaller production cross sections, the larger intrinsic width of the Higgs boson and, to a

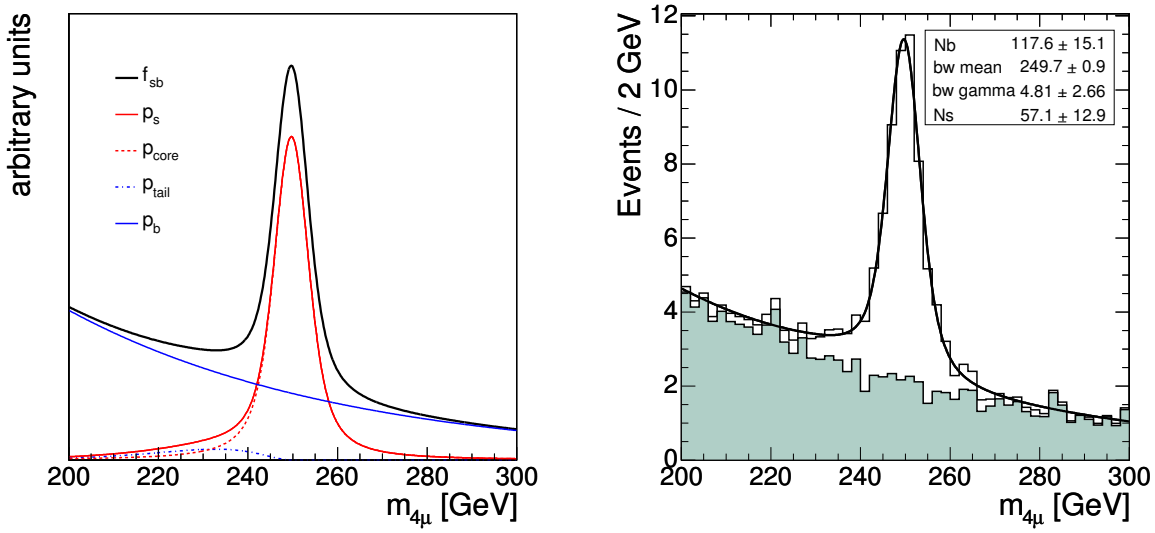


Figure 3.9: (Left) Example of the shapes of the different contributions to $f_{sb}$. (Right) Data-like distribution expected for a Higgs boson signals of $m_{\mathrm{H}} = 250\,\mathrm{GeV/c^2}$, for an integrated luminosity of $30\,\mathrm{fb}^{-1}$, together with the result of the fit (solid line) and the expected background (shaded area). This pseudo-experiment is selected randomly.

lesser extent, the worse resolution for high $p_T$ muons.

The number of signal and background events is obtained from the fit. The relative error in the cross-section measurement is determined from the number of signal events ($N_s$) and its statistical uncertainty ($\Delta N_s$) as $\Delta N_s/N_s$, shown in Figure 3.11 (left) as function of the Higgs boson mass. The contribution of the background is properly taken into account, as its normalisation is a free parameter in the fit. The cross section can be determined with a precision between 20% and 45%, except for masses below $130\,\mathrm{GeV/c^2}$, where the statistics is low.

The measured width, together with its statistical error, is presented in Figure 3.11 (right) as function of the true mass. The width can be determined with an error between 35% and 45% above $190\,\mathrm{GeV/c^2}$. Below this mass there is no sensitivity to the Higgs boson width and upper limits at 95% confidence level (C.L.) are set. For the sake of comparison, the width obtained by fitting only a Gaussian for masses below $200\,\mathrm{GeV/c^2}$ and only a Breit-Wigner for masses above $200\,\mathrm{GeV/c^2}$ is also shown, together with the statistical uncertainty. The Breit-Wigner-only fits do not take into account the detector resolution, and therefore the intrinsic theoretical values are not recovered.

The measurement of the parameters is affected by systematic uncertainties in the muon momentum resolution (determined from data), in the muon reconstruction efficiency (around 2%) and those associated to the selection cuts (close to 1%) [51]. These systematic uncertainties are mostly uncorrelated. The impact in the measured mass and width is small. The cross-section measurement is also affected by the uncertainty in the luminosity determination, which is around 3% (Figure 3.11 (left)).

The results obtained for Higgs boson masses around $170\,\mathrm{GeV/c^2}$ and above $500\,\mathrm{GeV/c^2}$, for which the expected number of events is somewhat low for $\mathcal{L} = 30\,\mathrm{fb}^{-1}$, have to be taken as representative results for the typical expected distributions. The higher errors of the para-

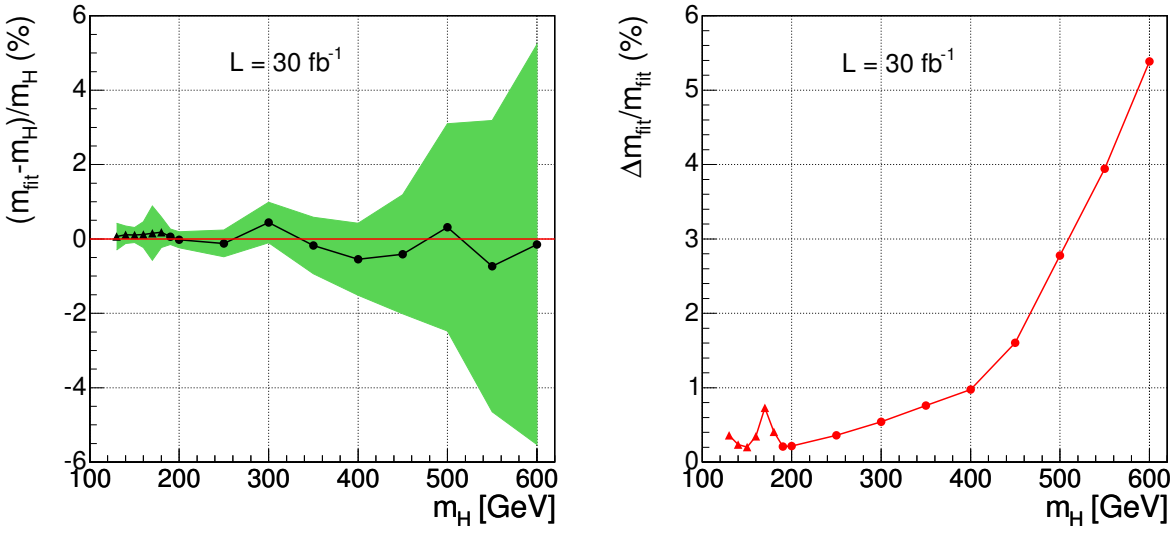


Figure 3.10: (Left) Relative shift of the fitted value of the Higgs boson mass with respect to the input $m_{\mathrm{H}}$ value, as function of $m_{\mathrm{H}}$. The shaded area is the error in the determination of the peak value from the fit, also shown as function of the Higgs boson mass (Right). The dots correspond to the result of the convolution and the triangles to the Gaussian approximation.

meters for those $m_{\mathrm{H}}$ values are consistent with statistics. For extending the measurement of the Higgs boson parameters to smaller masses or to lower luminosities, it should be more appropriate to extract the parameters from a large set of randomly chosen four-muon mass distributions with the correct statistics.

### 3.1.5 Conclusions

Discovery of the Standard Model Higgs boson and measurement of its mass, production cross section and width in the "golden" decay mode $\mathrm{H} \rightarrow \mathrm{ZZ}^{(*)} \rightarrow 4\mu$ were analysed with the CMS Detector. The explored range of Higgs boson masses was 115 GeV/c$^2$–600 GeV/c$^2$. The Monte Carlo samples were normalised to represent the NLO cross sections, including $\mathrm{m}_{4\mu}$-dependent K-factors. To simulate the detector response and reconstruct physics objects, the full CMS Detector simulation and reconstruction software was used. The Higgs boson discovery potential was explored for different analysis variations, including the use of $\mathrm{m}_{4\mu}$-dependent and flat cuts, log-likelihood ratio based on the full $\mathrm{m}_{4\mu}$ spectrum and a straightforward counting experiment approach. A full treatment of the most important theoretical and instrumental systematic errors and their effect on evaluation of significance of the Higgs boson observation as well as measuring its parameters were presented. To minimise systematic errors, a number of methods of reconstructing the necessary corrections directly from data were developed.

It was shown that at $\sim 2\,\mathrm{fb}^{-1}$ of integrated luminosity, CMS would be able to start excluding the Standard Model Higgs boson at 95% CL for $m_{\mathrm{H}}$ in vicinity of 200 GeV/c$^2$. By the time CMS reaches $\sim 30\,\mathrm{fb}^{-1}$, it would exclude the Standard Model Higgs boson in its four-muon decay mode in the mass range $m_{\mathrm{H}} = 120$ GeV/c$^2$-600 GeV/c$^2$, if indeed it does not exist.

The discoveries at the level of "$5\sigma$" local significance could be already possible at $\sim 10\,\mathrm{fb}^{-1}$ for $m_{\mathrm{H}}$ in the range 140 GeV/c$^2$-150 GeV/c$^2$ and 190 GeV/c$^2$-400 GeV/c$^2$. By the time $\sim 30\,\mathrm{fb}^{-1}$

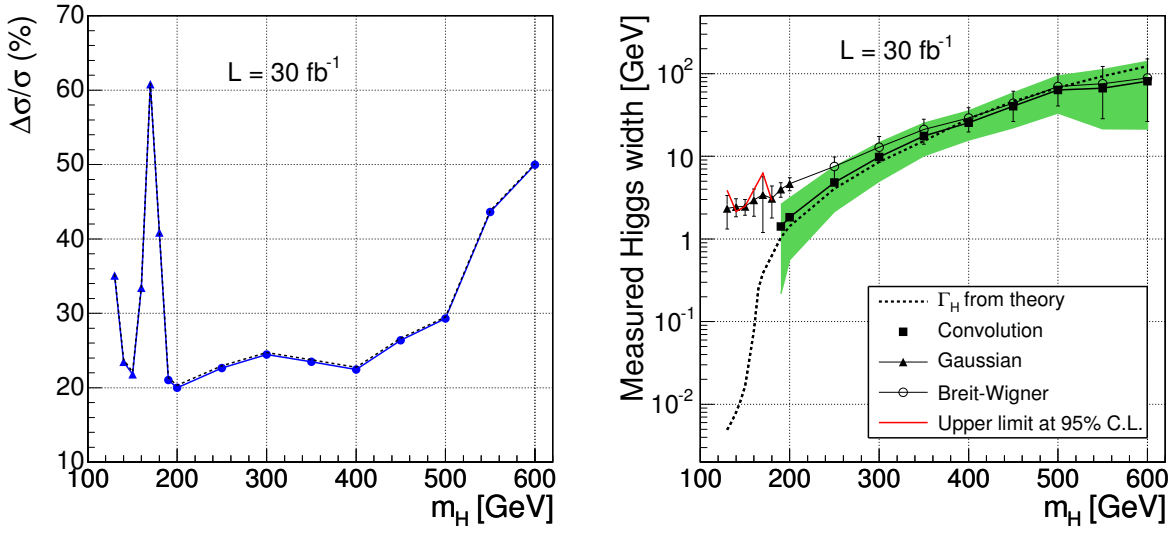


Figure 3.11: (Left) Relative error in the cross-section measurement, $\Delta N_s/N_s$, as a function of the $m_{\mathrm{H}}$. $\Delta N_s$ is the statistical error of $N_s$ obtained from the fit. The dots correspond to the result of the convolution and the triangles to the Gaussian approximation. The dashed line indicates the impact of the systematic uncertainties. (Right) Measured Higgs boson width (squares), its statistical error (green band) and the theoretical calculation of $\Gamma_{\mathrm{H}}$ (dashed line). Upper limits to the width at 95% C. L. are shown (red line) for $m_{\mathrm{H}} < 190\,\mathrm{GeV/c^2}$. The result of Gaussian (triangles) and Breit-Wigner (dots) fits are also shown for comparison.

are collected, the discovery range would open up to 130 GeV/c$^2$-160 GeV/c$^2$ and 180 GeV/c$^2$-500 GeV/c$^2$. An observation of the Higgs boson with the mass $m_{\mathrm{H}} \sim 170\,\mathrm{GeV/c^2}$ or $\sim 600\,\mathrm{GeV/c^2}$ in the $\mathrm{H} \rightarrow \mathrm{ZZ}^{(*)} \rightarrow 4\mu$ decay channel would require an integrated luminosity of the order of 100 fb$^{-1}$.

At the integrated luminosity of $\sim 30\,\mathrm{fb}^{-1}$, the Higgs boson mass could be measured with a precision between 0.1 % and 5.4 %, depending on its mass. The intrinsic width could be measured only for the Higgs boson heavier than 190 GeV/c$^2$, with a precision $\sim 35\%$. For lower masses, the Higgs boson width becomes much smaller than the detector resolution and only upper limits of the order of a few GeV could be set. The production cross section would be determined with a precision $\sim 30\%$.

## 3.2 Benchmark Channel: $H \rightarrow WW^{(*)} \rightarrow 2$ muons

### 3.2.1 Introduction

Previous studies [66, 67] demonstrated the relevance of the $H \rightarrow WW^{(*)} \rightarrow 2l2\nu$ channel for the Higgs discovery with an integrated luminosity of less than 5 fb$^{-1}$. The physics study was performed on the data produced at the end of the full simulation, trigger and off-line detector reconstruction chain, including realistic assumptions for the sub-detectors misalignments. The goal of this study is to provide the discovery potential as a function of the Higgs mass using detailed simulation reconstruction code, considering all the relevant background contributions and providing an as much as possible complete estimation of the systematic errors. The muon reconstruction has an average efficiency in the detector geometrical ac-

ceptance ($\eta < 2.4$) of $95 - 99\%$ for the transverse momentum ranging from 5 GeV/c up to $P_T = 1$ TeV/c, as extensively discussed in [7], while the fraction of mis-assigned charge for muons with $P_T = 100$ GeV/c is less than 0.1%.

### 3.2.2 Physics processes

#### 3.2.2.1 Signal processes

The signal was studied in the range between 130 to 180 GeV using 7 samples of datasets (Tab. 3.1). The generation was done using the PYTHIA program [68], considering the most relevant signal sources:

$$g\,g \rightarrow H \rightarrow WW^{(*)} \rightarrow 2\mu 2\nu \tag{3.1}$$

$$q\,\bar{q} \rightarrow VVq'\,\bar{q}' \rightarrow Hq'\,\bar{q}' \;\;;\;\; H \rightarrow WW^{(*)} \rightarrow 2\mu 2\nu \tag{3.2}$$

In the simulation, digitisation and reconstruction the effect of the event pile up expected at the machine luminosity $2 \times 10^{33}$cm$^{-2}$sec$^{-1}$ was included.

#### 3.2.2.2 Background processes

The dominant background giving the largest contribution at the end of the complete selection chain, is the irreducible one from the continuum production of W pairs decaying into muons and neutrinos. Other significant or critical sources of backgrounds are the production of top quarks and the Drell-Yan muon pairs. The most important backgrounds are thus the processes:

$$q\,\bar{q} \rightarrow W^+W^- \rightarrow 2\mu 2\nu \tag{3.3}$$

$$g\,g \rightarrow t\,\bar{t} \rightarrow 2\mu 2\nu \tag{3.4}$$

$$q\,\bar{q} \rightarrow \gamma^*, Z \rightarrow 2\mu \tag{3.5}$$

Further contributions from $b\bar{b}$, $ggWW$ , $WZ$, $ZZ$, and $Wt$ production processes were also considered. A part from $Wt$ and $gg \rightarrow WW$, all the processes have been generated with PYTHIA. For the former process, the TOPREX Monte Carlo [44] has been used which correctly takes into account the top mass and the spin correlations throughout the decay chain. The latter dataset has been simulated starting from a Monte Carlo sample produced by N. Kauer et al. [69]. The full list of dataset samples used for the background study is given in Tab. 3.2

#### 3.2.2.3 Cross sections at NLO

All the processes considered in this study have been simulated with LO accuracy. In order to approximate the NLO predictions for the signal and the W-pair background, phase space depended reweighting K-factors has been applied [70]. These factors have been obtained by matching respectively the $p_{\mathrm{T}}$ distribution of the Higgs and of the $W^+W^-$ system provided by PYTHIA to the one predicted by MC@NLO [71][1]. The K($p_{\mathrm{T}}$) factors used for each $p_{\mathrm{T}}$ intervals are given in Appendix of [72]. The absolute cross sections for Higgs production through gluon-gluon fusion and vector boson fusion have been calculated [20] and are listed in Tab. 3.1.

[1]For the signal, only the Higgs production through the gluon-gluon mechanism has been reweighted with K($p_{\mathrm{T}}$) factors accordingly to NLO description

Table 3.1: The cross section at the next-to-leading order for Higgs production through gluon fusion and vector boson fusion (VFB) processes and the number of generated events are reported.

| Higgs mass ( GeV/c$^2$) | $\sigma^{NLO} \times BR(2l)$ Gluon Fusion (pb) | $\sigma^{NLO} \times BR(2l)$ VBF (pb) | $\sigma^{NLO} \times BR(2l)$ num. of events |
|---|---|---|---|
| 130 | 0.94 | 0.12 | 20000 |
| 140 | 1.39 | 0.19 | 20000 |
| 150 | 1.73 | 0.25 | 17000 |
| 160 | 2.03 | 0.31 | 44000 |
| 165 | 2.04 | 0.32 | 49000 |
| 170 | 1.95 | 0.31 | 40000 |
| 180 | 1.71 | 0.28 | 20000 |

No reweighting has been applied to the other processes, whose total cross sections have been simply rescaled accordingly the NLO calculation performed sing the MCFM Monte Carlo program [55, 73, 74]. These cross sections are reported in Tab. 3.2.

Table 3.2: The cross section at the next-to-leading order for the background processes. The $gg \rightarrow WW$ process is generated using a matrix element program linked to PYTHIA for the showering [69]. This process is only known at LO. (*) For $b\bar{b} \rightarrow 2\mu$ the pre-selection $p_T > 20, 10$ GeV/c was applied.

| Channel | $\sigma^{NLO} \times BR(pb)$ | num. of ev. |
|---|---|---|
| $qq \rightarrow WW \rightarrow 2l$ | 11.7 | 164000 |
| $t\bar{t}$ | 840 | 548000 |
| $gg \rightarrow WW \rightarrow 2l$ | 0.54 (LO) | 50000 |
| $\gamma^*, Z$ | 145000 | 2700000 |
| $b\bar{b} \rightarrow 2\mu$ | 710 (LO)(*) | 640000 |
| $ZW \rightarrow 3l$ | 1.63 | 72000 |
| $tWb \rightarrow 2l$ (TOPREX) | 3.4 | 191000 |
| $ZZ \rightarrow 2l$ | 1.52 | 99000 |

### 3.2.3 Event selection

The signal selection requires the identification of two high $p_T$ isolated muons. The background reduction is obtained applying suitable kinematic cuts to the reconstructed muons, a veto on the presence of central jets and a high missing $E_T$ (MET) in the event. As discussed in the following sections, separate optimisations were performed independently on the muon isolation variables, jet and missing energy thresholds and on the muons kinematical variables.

### 3.2.4 The trigger selection

Events passing the global Level-1 trigger must be reduced with a more restricted trigger requirement to limit the recorded event rate. Two trigger streams were considered in this analysis:

1. the HLT double muon stream;

2. the OR of the HLT single muon and double muon stream.

Before any selection the single or double muon HLT trigger efficiency is 92 %, while the double muon HLT trigger efficiency is 80 % [75]. After the off-line cuts for the Higgs selection, which will be described in detail in the following section, the overall efficiency of the first stream relative to the second one is found to be $(97 \pm 1)$%, for $m_H = 165\,\mathrm{GeV/c^2}$. In the following, the trigger selection used was the HLT double muon stream, for which the trigger rate is predicted to be a factor $\sim$7 smaller than the single muon one [75].

#### 3.2.4.1 The muon identification and isolation

A first event selection based on the identification of two prompt muons required :

- Level-1 and HLT dimuon trigger bits found;
- two oppositely charged muons reconstructed by the Global Muon reconstructor algorithm developed in ORCA, as described in [7].

The first requirement assures the events to be found in the CMS dimuon data stream, which currently foresees a symmetric threshold of 7 GeV/c on the $p_T$ of both muons as reconstructed by the High Level Trigger algorithm, for operations at a machine luminosity of $2 \times 10^{33}\mathrm{cm^{-2}s^{-1}}$; in addition, at least one of the muons must fulfill the HLT isolation criteria [75]. As discussed in ref.[75], the trigger rate for this datastream is predicted to be about 4 Hz.

At the off-line reconstruction and selection stage, two cones were considered for the isolation around each reconstructed muon tracks. The $\sum P_T$ summed over all the charged track candidates found in the Tracker detector was accounted inside the first cone. The $\sum Et$ over the energy deposits in the ECAL and HCAL towers was accounted in the second cone. The size of a cone around a muon track is defined as $\Delta R = \sqrt{\Delta\eta^2 + \Delta\phi^2}$. A muon is considered to be isolated if the $\sum Pt$ ($\sum Et$) inside the considered cones of size $\Delta R_{Tracker}$ ($\Delta R_{Calo}$) is below the threshold $P_T$ (max) ($E_T$ (max)). An optimisation study was performed to find the four parameters:

$$(1)\ \ \Delta R_{Tracker} \quad (2)\ \ P_T\ \text{(max)} \quad (3)\ \ \Delta R_{Calo} \quad (4)\ \ E_T\ \text{(max)}$$

searching for the highest signal over background ratio. The optimisation was performed using the signal dataset with $m_H = 165\,\mathrm{GeV/c^2}$ and the $b\bar{b}$ background dataset, which is the most sensitive to the isolation cut. At this first stage of the selection, the background reduction was not requested to be very large, thus keeping the signal reduction relatively small; for each combination of the cones:

$$\Delta R_{Tracker} = 0.25,\ 0.3,\ 0.35,\ 0.4 \quad \Delta R_{Calo} = 0.25,\ 0.3,\ 0.35,\ 0.4 \tag{3.6}$$

the cut efficiency of 85% for the signal was requested. With two free parameters, $E_T$ (max) and $P_T$ (max), several solutions are possible. A reasonable choice is to give the same weight to the Tracker and Calorimeter isolation cuts. The mean and the r.m.s. values of the $p_T$ and energy deposition for the signal dataset within different cones are reported in [76]. For each set of isolation cones ($\Delta R_{Tracker}$,$\Delta R_{Calo}$ ) the $E_T$ and $P_T$ thresholds were chosen as follows:

$$E_T^{thresh} =< E_T > + x \cdot \sigma(E_T) \tag{3.7}$$

$$P_T^{thresh} =< P_T > +x \cdot \sigma(P_T) \tag{3.8}$$

where the parameter $x$ was set to the value giving the required $85\%$ efficiency for the signal. Fig. 3.12 shows the resulting background selection efficiency.

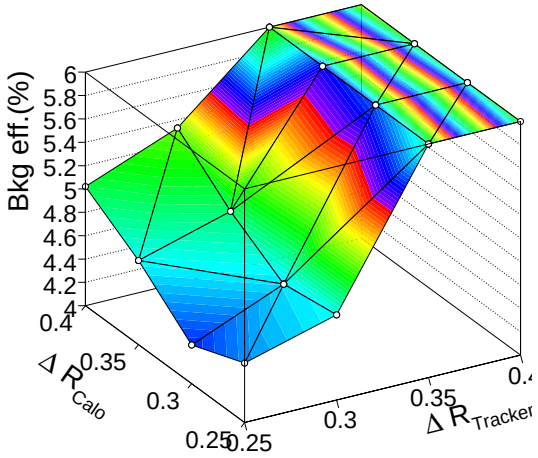


Figure 3.12: $b\bar{b}$ background efficiencies for the 16 combinations of cones considered for the muon isolation selection cut.

The best selection is obtained with:

$$\Delta R_{Tracker} = 0.25 \quad P_T < 2.0\,\text{GeV/c} \quad \Delta R_{Calo} = 0.3 \;\; E_T < 4.7\,GeV \tag{3.9}$$

corresponding to $x = 1.8$ for the energy deposition and $P_T$ cut. The isolation cuts used in the analysis were:

$$\Delta R_{Tracker} = 0.25 \quad P_T < 2.0\,\text{GeV/c} \quad \Delta R_{Calo} = 0.3 \;\; E_T < 5.0\,\text{GeV} \tag{3.10}$$

### 3.2.5 Jet reconstruction and the jet veto

The reconstruction of jets is needed to obtain a strong $t\bar{t}$ background reduction by applying a jet veto. The jet reconstruction algorithms can use the raw energy sum of the ECAL and HCAL towers, either with a fixed energy threshold or with $\eta$-dependent thresholds. The $\eta$-dependent threshold does not improve the $t\bar{t}$ background rejection with respect to a fixed combined $E_T$ and $E$ thresholds [72]. The jets reconstructed from raw energies with fixed $E_T$ and $E$ thresholds were finally chosen to be used for the JET veto. A strong $E_T$ cut helps in the background reduction. However, below $E_T = 25\,\text{GeV}$ the fraction of jets matching with a generated jet starts to decrease, because of ghost jet candidates mainly due to pileup events. The matching was defined within a cone around the reconstructed jet candidate $\Delta R_{rec-gen\ jet} < 0.3$. In order to reduce the number of fake jets, a quality parameter was introduced:

$$\alpha = \sum_{selected\ tracks} P_T/E_T(jet) \tag{3.11}$$

where the selected tracks are those inside the jet ($\Delta R_{trk-jet} < 0.5$) with more than 5 associated hits, pointing to the primary interaction vertex ($|z_{trk} - z_{vtx}| < 0.4\,\text{cm}$). The mean

value of $\alpha$ is 0.66 (two third of the jet energy on average is due to charged particles). A reconstructed jet candidate with $E_T$ in the low energy region ($< 20\,\text{GeV}$) was considered only if $\alpha > 0.2$. It has been shown [72] that this selection significantly reduces the number of fake jets ( the fraction of matched jets being greater than $90\%$ for $E_T > 15\,\text{GeV}$ ) with negligible loss of reconstruction efficiency for true jets. Different jet reconstruction algorithms were tested. The best signal ($m_H = 165\,\text{GeV/c}^2$) / background ($t\bar{t}$) ratio was obtained using an iterative cone algorithm [77] with a cone size R= 0.5 and calorimeter towers having raw energies $E_T^{tower} > 0.5\,\text{GeV}$ and $E^{tower} > 0.8$. To summarise, the jet veto is applied if:

$$E_T > 15\,\text{GeV} \qquad |\eta_{jet}| < 2.5 \tag{3.12}$$

and the $\alpha$ cut is required in the jet energy range $15\,\text{GeV} < E_T < 20\,\text{GeV}$.

### 3.2.6 Missing energy reconstruction and the MET cut

The transverse missing energy is reconstructed with the sum of the ECAL and HCAL tower raw energies, corrected for the muons energy contribution. The most sensitive background to the MET cut is the dimuon production from Drell-Yan (DY) process. The right plot in Fig. 3.13 shows the MET distributions for DY events having a reconstructed dimuon invariant mass inside the Z mass region (shown by the black area in the left plot), and for signal events with $m_H = 165\,\text{GeV/c}^2$. The signal and background distribution were normalised to an integrated luminosity $\mathcal{L} = 10\,\text{fb}^{-1}$.

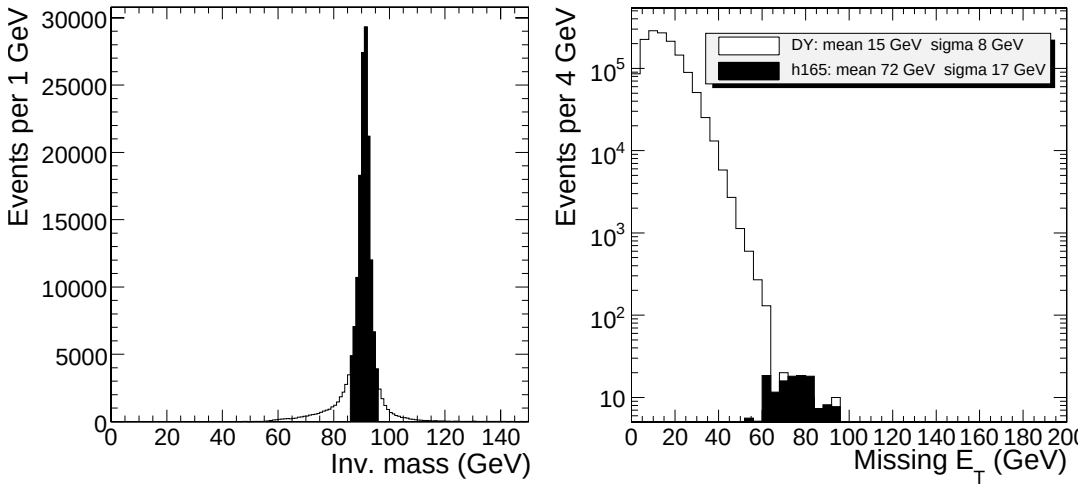


Figure 3.13: Reconstructed dimuon invariant mass for Drell-Yan events selected inside the Z mass region(left, black area); MET distributions for the selected Drell-Yan events and for signal events scaled at the integrated luminosity $\mathcal{L} = 10\,\text{fb}^{-1}$ (right).

A MET threshold of $47\,\text{GeV}$ is $4\sigma$ over the mean value for the background and $1.5\sigma$ under the mean value for the signal. Drell-Yan events are thus strongly suppressed by applying a MET threshold. The cut used in this analysis was MET $> 50\,\text{GeV}$.

#### 3.2.6.1 The kinematic cuts

The kinematic of the two muons is different for signal and background:

- signal events from gluon-gluon scattering are more central than the $W^+W^-$ background from $q\bar{q}$ scattering, thus resulting in a slightly more central rapidity distribution for the decay muons;

- due to the scalar nature of the Higgs boson and of the V-A structure of the weak interaction, for Higgs masses close to $2 \cdot M_W$, the $W^+W^-$ spin correlation plays in favour of small opening angles between the two muons;
- signal events have a lepton $P_T$ spectra peak close to $M_W/2$;
- DY background has a two muons invariant mass peak at $M_Z$.

In addition , the muons from b quarks (as in the case of the $b\bar{b}$ background and eventually from $t\bar{t}$ ) have large impact parameters. The following cuts were applied before the optimisation of the kinematical cuts:

1. $|\eta(\mu_1))|$ , $|\eta(\mu_2)| < 2.0$ (pseudorapidity of the two muons);
2. $IP(\mu_1)$ , $IP(\mu_2) < 3\sigma$ (impact parameter of the two muons);
3. $P_T(\mu_{max}) < 55\,\text{GeV/c}$ (transverse momentum of the two muons);
4. $m_{\mu_1\mu_2} > 12\,\text{GeV/c}^2$ (invariant mass of the two muons);
5. $\Delta\phi_{\mu_1\mu_2} < 0.8$ (opening angle between the two muons).

Cut 1 is useful for the WW background reduction, as well as cuts 3 and 5. Cut 2 reduces the $b\bar{b}$ events, while cut 4 rejects potential background from b-resonances. After the requirement of the muon isolation described before, the overall signal efficiency for cuts 1 to 4 is about $90\%$. The distribution of the variable $\Delta\phi_{\mu_1\mu_2}$ will be used to search for the Higgs signal.

The optimisation study was performed by varying the following cuts:

$$P_T(\mu_{max}) > 25, 30, 35, 40\,\text{GeV/c} \quad P_T(\mu_{min}) > 15, 20, 25, 30\,\text{GeV/c}^2 \tag{3.13}$$

$$m_{\mu_1\mu_2} < 35, 40, 45, 50, 55, 60\,\text{GeV/c}^2 \tag{3.14}$$

to find the set of cuts giving the best significance. The estimator $S_{cP}$ was used, which gives the significance using the Poisson distribution [78]. The input of the estimator are the number of signal and background events, the statistical uncertainties and the theoretical systematics in the background. The optimisation was performed using as before the signal dataset with $M_H = 165\,\text{GeV/c}^2$, and using all the background contributions, properly normalised considering their production cross sections.

The optimisation result could depend on the statistics of the event data samples and on the estimated systematic errors. We searched for the maximum significance in four different conditions:

$$\mathcal{L} = 1\,\text{fb}^{-1} \quad \mathcal{L} = 2\,\text{fb}^{-1} \quad syst.\,err. = 10\% \quad syst.\,err. = 15\% \tag{3.15}$$

Fig. 3.14 shows, as an example, the significance expected as a function of $p_T(\mu_{max})$ and $p_T(\mu_{min})$ cuts for two different values of the dimuon invariant mass cut, for the case of an integrated luminosity $L = 1\,\text{fb}^{-1}$ and an overall $10\%$ systematic error.

The following cuts:

$$P_T(\mu_{max}) > 35\,\text{GeV/c} \quad P_T(\mu_{min}) > 25\,\text{GeV/c} \quad m_{\mu_1\mu_2} < 50\,\text{GeV/c}^2 \tag{3.16}$$

give the maximum significance (about 3.0 for $\mathcal{L} = 1\,\text{fb}^{-1}$ and an assumed syst. err. $= 10\%$) in all the four conditions.

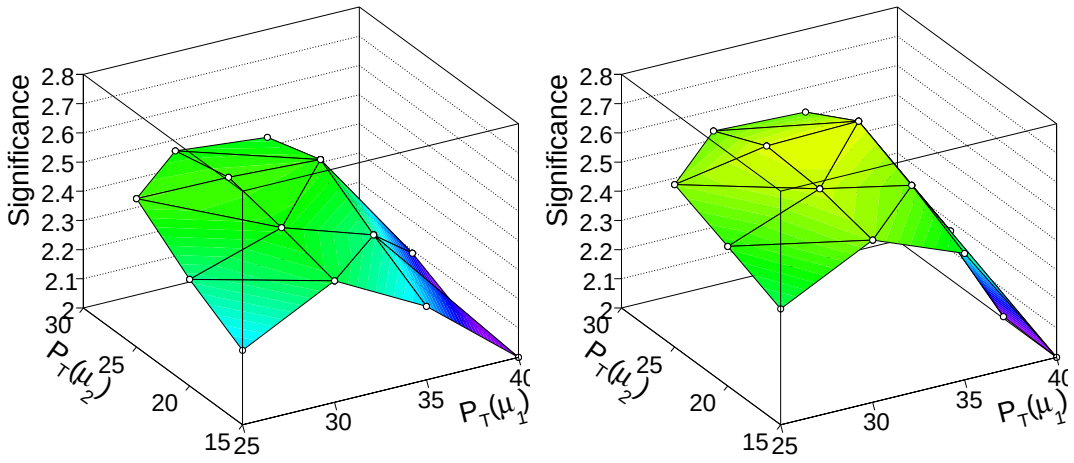


Figure 3.14: Significance as a function of $P_T$ cuts for $m_{\mu_1\mu_2} < 40\,\text{GeV/c}^2$ (left) and for $m_{\mu_1\mu_2} < 50\,\text{GeV/c}^2$ (right) with $\mathcal{L} = 1\,\text{fb}^{-1}$ and syst. err. $= 10\%$

### 3.2.7 The selection results

The optimised selection cuts discussed above were applied to the background and signal samples. The list of cuts is described in Tab. 3.3. The expected number of events for a luminosity of 1 $\text{fb}^{-1}$ are given in Tab. 3.4 for the signals and the backgrounds.

Table 3.3: The list of cuts applied to the signal and background samples

| | | | |
|---|---|---|---|
| 1 | L1+HLT dimuon | 6 | MET$> 50\,\text{GeV}$ |
| 2 | 2 $\mu$ opposite charge | 7 | $35\,\text{GeV/c} < P_T(\mu_{max}) < 55\,\text{GeV/c}$ |
| 3 | Isolation | 8 | $25\,\text{GeV/c} < P_T(\mu_{min})$ |
| 4 | $\eta < 2.0 \quad IP < 3\sigma$ | 9 | $m_{\mu_1\mu_2} < 50\,\text{GeV/c}^2$ |
| 5 | Jet Veto | 10 | $\Delta\phi_{\mu_1\mu_2} < 0.8$ |

Figure 3.15 shows the distributions of the MET, $P_T(\mu_{max})$, $P_T(\mu_{min})$ and $m_{\mu 1\mu 2}$ variables for the signal and the three most important backgrounds after the jet-veto and the following selection cuts applied in the order reported in the Tab. 3.3.

Figure 3.16 shows the final distribution obtained for the azimuth angle difference between the muons, expected for an integrated luminosity $\mathcal{L} = 10\,\text{fb}^{-1}$ and for the Higgs signal of mass $m_H = 165\,\text{GeV/c}^2$.

As stated above, all the numbers at the various selection steps refer to the analysis applied to the HLT dimuon stream. For comparison the event numbers after all the selection cuts were also studied for the case in which the analysis were performed on the data including the single muon trigger data stream. The inclusion of this datastream, which is foreseen to have a rate about 7 times larger than the dimuon stream [75], would result in a $(3 \pm 1)\%$ increase of the overall signal selection efficiency. The Higgs search with mass appreciably different than $165\,\text{GeV/c}^2$ can take advantage from a dedicated cut optimisation, such as the one reported in [76].

Table 3.4: The expected number of events for a luminosity of 1 fb$^{-1}$ for the signal with Higgs masses between 130 and 180 GeV/c$^2$ and for the backgrounds.

| | L1+HLT dimuon | All cuts | $\epsilon_{tot}$ |
|---|---|---|---|
| $m_H = 130\,\text{GeV/c}^2$ | 112 | $0.68 \pm 0.19$ | $(0.07 \pm 0.02)\%$ |
| $m_H = 140\,\text{GeV/c}^2$ | 162 | $1.7 \pm 0.4$ | $(0.12 \pm 0.03)\%$ |
| $m_H = 150\,\text{GeV/c}^2$ | 228 | $5.3 \pm 0.8$ | $(0.26 \pm 0.04)\%$ |
| $m_H = 160\,\text{GeV/c}^2$ | 256 | $12.6 \pm 0.7$ | $(0.58 \pm 0.04)\%$ |
| $m_H = 165\,\text{GeV/c}^2$ | 264 | $14.3 \pm 0.8$ | $(0.64 \pm 0.04)\%$ |
| $m_H = 170\,\text{GeV/c}^2$ | 259 | $11.0 \pm 0.7$ | $(0.53 \pm 0.03)\%$ |
| $m_H = 180\,\text{GeV/c}^2$ | 233 | $5.9 \pm 0.8$ | $(0.30 \pm 0.04)\%$ |
| $qq \rightarrow WW$ | 1040 | $4.1 \pm 0.5$ | $(0.036 \pm 0.005)\%$ |
| $t\bar{t} \rightarrow 2\mu 2\nu$ | 17007 | $2.6 \pm 0.3$ | $(0.012 \pm 0.001)\%$ |
| $gg \rightarrow WW$ | 58 | $1.0 \pm 0.1$ | $(0.18 \pm 0.02)\%$ |
| $\gamma^*, Z \rightarrow 2\mu$ | 720653 | $0.3 \pm 0.3$ | $(4 \pm 4)10^{-5}\%$ |
| $b\bar{b} \rightarrow 2\mu 2\nu$ | 69374 | 0 | $0\%$ |
| $Wt$ | 615 | $0.57 \pm 0.10$ | $(0.017 \pm 0.003)\%$ |
| $ZZ$ | 218 | $0.18 \pm 0.05$ | $(0.012 \pm 0.003)\%$ |
| $ZW$ | 384 | $0.13 \pm 0.05$ | $(0.008 \pm 0.003)\%$ |

### 3.2.8 Background estimation and systematics

The precise understanding of the backgrounds is the most critical issue concerning this Higgs discovery channel. The direct use of the Monte Carlo predictions, i.e. $N_{bkg,MC} = \sigma_{bkg,MC} \cdot \varepsilon_{ff}$, leads to high systematic uncertainties due either to theoretical calculation and to experimental systematics. The most reliable approach to address this problem is to measure the different sources of background directly from the data. The commonly used method to extrapolate the background contribution directly from the data consists of selecting a signal-free phase space region (control region) where a given background process is enhanced. The normalisation from data for the two most relevant background, i.e. $t\bar{t}$ and $WW$ has been addressed. For both backgrounds, a dedicated control region was defined. The number of background events in the signal region can then be estimated through:

$$N_{signal\_reg} = \frac{N^{MonteCarlo}_{signal\_reg}}{N^{MonteCarlo}_{control\_reg}} N_{control\_reg} \tag{3.17}$$

where $N^{MonteCarlo}_{signal\_reg}$ and $N^{MonteCarlo}_{control\_reg}$ are the numbers of events predicted by the Monte Carlo simulation in the signal and control region. The error on the ratio $N^{MonteCarlo}_{signal\_reg}/N^{MonteCarlo}_{control\_reg}$ accounts for a theoretical contribution (scale variation, PDF uncertainty) and detector systematics effects. The precision with which the number of $N_{signal\_reg}$ can be predicted depends also on the statistical error on $N_{control\_reg}$.

### 3.2.9 $t\bar{t}$ background normalisation

Since the presence of two b-tagged jets is a striking evidence for $t\bar{t}$ events, the most natural control region for this process is then defined by applying the same selection cuts as for the signal region but the jet veto, with the additional request of two b-tagged jets in the detector

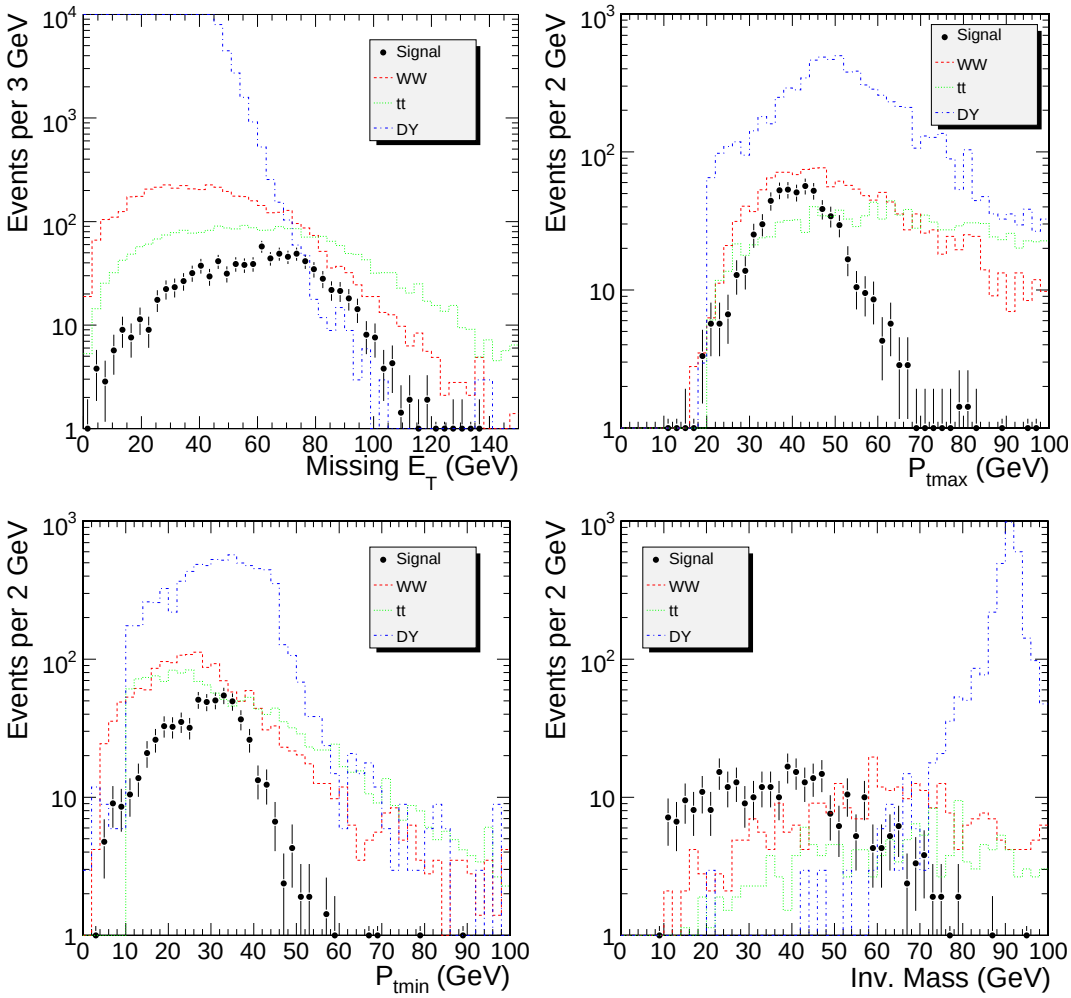


Figure 3.15: Distributions of the missing energy, transverse momentum and invariant mass for a luminosity of 10 fb$^{-1}$ following the cut list order.

acceptance[2]. The $t\bar{t}$ evaluation from the data for the $H \rightarrow WW^{(*)}$ channel has been studied in Ref. [79] to which we refer for further details. In this study a jet is tagged as a b-jet if its measured $E_{\mathrm{T}}$ is greater then 20 GeV and if there are at least two tracks belonging to the jet (i.e. within a cone of 0.5 around the jet axis) whose $\sigma_{\mathrm{IP}}$ is higher than 2. With such settings the double b-tagging efficiency for $t\bar{t}$ events is $\mathcal{O}(30\%)$. The mis-tagging rate has been calculated from the ratio between the number of b-tagged jets and the total number of jet with $E_T > 20$ GeV in the fully simulated DY sample and it resulted to be $\mathcal{O}(3\%)$.
In the following we consider the background processes in the $t\bar{t}$ control region. For 1 fb$^{-1}$ the number of $t\bar{t}$ events in the control region just defined is foreseen to be 17, whereas the contribution from the signal and $Wt$ is completely negligible (in both cases smaller than 0.1 events).

Not all the processes with $2\mu + 2b + E_t^{miss}$ as final state have been fully simulated for this analysis, nevertheless general considerations and fast Monte Carlo generator level cross

[2] in Ref. [79] an additional control region for $t\bar{t}$ events defined by requiring two high $E_{\mathrm{T}}$ jets instead of two b-tagged jets has been proposed. However, it has been shown there that due to the high contamination from Drell-Yan events, this control region is less indicate for same flavour lepton final states

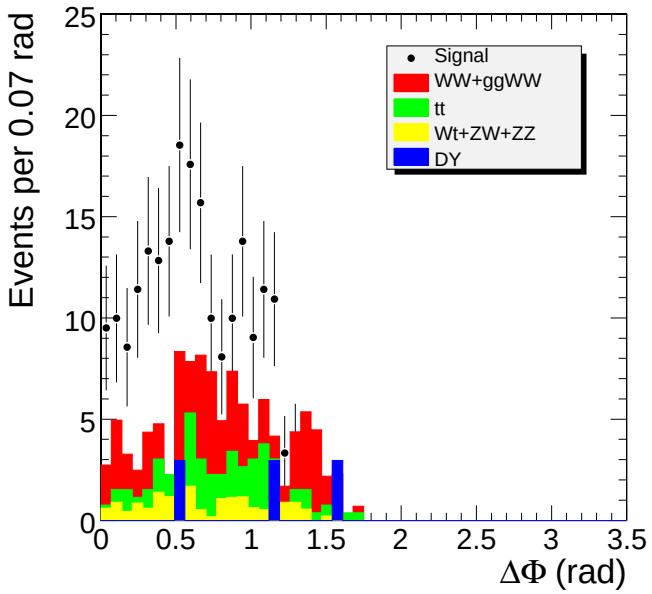


Figure 3.16: Distribution of the angle between the two muons for a luminosity of 10 fb$^{-1}$ at the end of the selection.

checks lead to exclude other sources of backgrounds, as briefly outlined in the following.
The more natural concurrent process is the non-resonant $W^+W^- \rightarrow 2\mu + b\bar{b}$ which is suppressed with respect to $t\bar{t}$. Its cross section is indeed expected to be smaller than $0.3$ $pb$. Assuming the same efficiency for the kinematic selections as for the $W^+W^- \rightarrow 2\mu$ ($\sim 0.07\%$) and including the double-b tagging efficiency, less than $0.1$ events are expected for 1 fb$^{-1}$ in the control region.
In the fully simulated Drell-Yan sample used in this analysis, the eventual additional $b\bar{b}$ pair comes only from a gluon splitting; the main mechanism of $\gamma^*/Z^* + 2b$ is not included. For an estimation of the contamination of the $t\bar{t}$ control region due to this process we thus used a parton level sample generated with a matrix element Monte Carlo (MADGRAPH [80]). Applying the signal kinematic selections, but the $E_T$ cut on the latter sample, $\sim 10$ events are expected for 1 fb$^{-1}$. The rejection due to $E_T$ cut has been calculated from the fully simulated sample where actually two b-quarks were present in the final state and it turned to be smaller than $1\%$. Considering also the efficiency for the double b-tagging, we can safely exclude this as a dangerous background.

In the following the various contribution of uncertainty in the $t\bar{t}$ normalization procedure are listed and described. The results are summarised in Table 3.5 for 1, 5 and 10 fb$^{-1}$.

- **Theoretical uncertainty.**

  The theoretical uncertainty of the $t\bar{t}$ cross section ratio $\sigma_{signal\_reg}/\sigma_{control\_reg}$ has been studied in [81] at parton level with LO precision by varying the reorganisation and factorisation scale. The error has been estimated to range between 3% to 10% mostly due to the choice of PDF. Some studies were done also at NLO: $E_T$ spectra and multiplicity of jets are not affected by higher order contributions but the estimate of the theoretical error at NLO is not available. In the following we will assume the theoretical uncertainty on the $t\bar{t}$ normalisation procedure to be 10%.

- **Jet Energy Scale (JES) uncertainty.**

  In the background normalisation procedures we proposed, the JES uncertainty is particularly important since it affects in an opposite sense the signal region, defined by vetoing the jets, and the control region where the presence of two jets is required. To take into account this sort of anti-correlation of $\epsilon_{\text{signal\_reg}}$ and $\epsilon_{\text{control\_reg}}$, we estimate the effect of the JES uncertainty directly on their ratio by rescaling the measured jet four momentum by a fractional uncertainty (i.e. $\mathrm{P}^{\mu}_{\text{jet}} = (1+\lambda)\mathrm{P}^{\mu}_{\text{jet}}$). The relative variation of $\frac{N^{MonteCarlo}_{signal\_reg}}{N^{MonteCarlo}_{control\_reg}}$ for various values of $\lambda$ is reported in [76]. The JES uncertainty foreseen at CMS is $\mathcal{O}(5\%)$ for 1 fb$^{-1}$ and it is expected to decrease down to $\sim 3\%$ for 5 fb$^{-1}$ (thanks to the calibration on the W mass) [7]. The effect of the JES uncertainty is $10\%$ for 1 fb$^{-1}$ and $6\%$ for 5 fb$^{-1}$.

- $\alpha$ **criterion uncertainty.**

  To estimate the systematic uncertainty due to $\alpha$ criterion, the value of the cut has been varied from 0.15 to 0.25. Moreover different values of the minimum $p_{\mathrm{T}}$ for a track to be included in the sum have been tried, from 2 to 3 GeV/c. The consequent variation of the jet veto efficiency (affecting only $N^{MonteCarlo}_{signal\_reg}$) is relatively small, i.e. of the order of 4%.

- **b-Tagging uncertainty.**

  The uncertainty on the b-tagging efficiency will be estimated exploiting $t\bar{t}$ events as calibration samples. The precision with which the b-tagging efficiency will be known is expected to be $\pm$ 11% for 1 fb$^{-1}$ integrated luminosity and it is foreseen to improve to $\pm$ 7% with 10 fb$^{-1}$ [82].

- **Uncertainties on the composition of the control region.**

  As it has been shown in the previous section, $t\bar{t}$ is the dominant process in the chosen control region, other processes contributing less than 1%. It is then safe to simply neglect this source of systematic error.

- **Statistical uncertainty on** $N_{control\_reg}$

  Assuming a Poissonian behaviour, the statistical uncertainty scales with the integrated luminosity as the square root of the number of $t\bar{t}$ events in the control region.

Table 3.5: Sources of uncertainty for the $t\bar{t}$ background normalisation procedure. Results are shown for 1, 5 and 10 fb$^{-1}$.

| Luminosity ( fb$^{-1}$) | Theoretical error | Detector systematics | | | Statistical error | Total error |
|---|---|---|---|---|---|---|
| | | JES | $\alpha$ criterion | b-tagging | | |
| 1 | 10% | 10% | 4% | 11% | 24% | 30% |
| 5 | 10% | 6% | 4% | 9% | 11% | 19% |
| 10 | 10% | 6% | 4% | 7% | 8% | 16% |

### 3.2.10 $WW$ background normalisation

In contrast to the $t\bar{t}$ background normalisation, which can be performed using an almost completely pure $t\bar{t}$ control sample, it is impossible to isolate the WW background in a clean

way, which means that contributions of other processes have to be subtracted and their systematic uncertainties have to be taken into account during the normalisation procedure of the WW background, including $\mathrm{gg} \to \mathrm{W^+W^-}$ events. In Fig. 3.17 the overall background normalisation strategy is illustrated. There are four phase space regions involved in the WW background normalisation. Each region is defined with a certain set of cuts:

- signal region: the selection of events in the signal region as described above.
- WW region: same as in the signal region, but $\Delta\phi_{\mu_1\mu_2} > 0.8$ and $50\,\mathrm{GeV/c^2} < m_{\mu 1\mu 2} < 80\,\mathrm{GeV/c^2}$.
- DY (WW) region: same as in the WW region, but $80\,\mathrm{GeV/c^2} < m_{\mu 1\mu 2} < 100\,\mathrm{GeV/c^2}$.
- $t\bar{t}$ (WW) region: same as in the WW region, but the jet veto is replaced with the requirement of two b-tagged jets ($E_t > 20\,\mathrm{GeV}$ and two tracks with $\sigma_{IP}$ >2).

In all cases, the selection is independent of the Higgs mass hypothesis. The total number of events in each region is given in Tab. 3.6, and the contributions of individual processes are represented in form of pie charts in Fig. 3.17. The main contamination of the WW region is due to Drell-Yan, $t\bar{t}$ and the Higgs signal. The number of Drell-Yan and $t\bar{t}$ is determined by extrapolating the corresponding numbers from relatively clean control regions and are subtracted from the WW region. Additional small contributions from other backgrounds in the WW region are determined from Monte Carlos and then subtracted. So far, no concrete method has been established to subtract Higgs events from the WW control region. Therefore, we choose the conservative approach to treat these Higgs events as an additional background in the WW region.

- **Theoretical uncertainties**

  The theoretical uncertainties of W pair production with subsequent decay to leptons have been studied in detail in Ref. [83], and the main sources of potential uncertainties of the shapes of kinematic variables turn out to be spin correlations, underlying event, and scale dependence. The effect of spin correlations can be taken into account properly with the correct choice of an event generator, and the underlying event is expected to be measured from the data with sufficient precision. The shape dependence on the choice of the reorganisation and factorisation scales is sizable in case of the contribution from the $\mathrm{gg} \to \mathrm{W^+W^-}$ subprocess, because the higher order corrections are unknown in this case. For the cuts, described below, this uncertainty is about 9% and is taken into account in the following.

- **Statistical error and uncertainties on the composition of the control region.**

  All background normalisation uncertainties are calculated in the following way:

$$\delta_{\mathrm{extrapolation}} = \sum_i \sqrt{n_{\mathrm{total}} + (n_i \times \delta_i)^2} \times \varepsilon_{\mathrm{control}\to\mathrm{target}} \tag{3.18}$$

  where $n_{\mathrm{total}}$[3] is the total number of events in the corresponding control region, $n_i \times \delta_i$ is the product of the number of events and the systematic uncertainty of an individual process in the control region, and $\varepsilon_{\mathrm{control}\to\mathrm{target}}$ is the extrapolation efficiency from the control region to the target region, e.g. the signal region.

The WW background normalisation requires three extrapolations from control regions to target regions:

[3] This term takes into account the statistical fluctuations of the control sample.

- DY (WW) region ⇒ WW `region`: with an extrapolation uncertainty of 5% [84] the extrapolated number of events and the uncertainty from Eq. 3.18 is 15.86 ± 1.23 events (79.29 ± 4.49 events) for 1 fb$^{-1}$ (5 fb$^{-1}$) of integrated luminosity.
- $t\bar{t}$ (WW) region ⇒ WW region: with an extrapolation uncertainty of 20% (15%) [79] the extrapolated number of events and the uncertainty from Eq. 3.18 is 6.19 ± 1.75 events (30.93 ± 5.41 events) for 1 fb$^{-1}$ (5 fb$^{-1}$) of integrated luminosity.
- WW region ⇒ signal region: as illustrated in Fig. 3.17, the first two items are inputs to this extrapolation, which means that the obtained numbers of Drell-Yan and $t\bar{t}$ events are subtracted in the WW region and the corresponding uncertainties are propagated. The extrapolation uncertainty of WW events, which is mainly due to the unknown higher order correction of the $\mathrm{gg} \to \mathrm{W^+W^-}$ contribution [83], amounts to 9% for the cuts used in this analysis. In addition, the remaining backgrounds a re estimated and subtracted with the following uncertainties: $\delta_{\mathrm{Wt}}$ = 40%, $\delta_{\mathrm{ZW}}$ = 20% and $\delta_{\mathrm{ZZ}}$ = 20%. According to Eq. 3.18 we obtain 7.35 ± 3.04 events (36.77 ± 7.85 events) for 1 fb$^{-1}$ (5 fb$^{-1}$) of integrated luminosity.

The results of the last item are used for the calculation of the Higgs discovery potential with $m_h$ = 165 GeV/c$^2$, and an integrated luminosity of either 1 fb$^{-1}$ or 5 fb$^{-1}$.

Furthermore, it should be pointed out that the entire background normalisation procedure is performed using only the dimuon data set and therefore no additional data sets are needed. In this way, potential uncertainties due to different trigger efficiencies and different integrated luminosities of other data sets do not play a role.

Table 3.6: Number of expected events in all the regions with an integrated luminosity of 1 fb$^{-1}$. The signal region numbers are referred to $m_H$=165 GeV/c$^2$.

| Channel | Signal region | $t\bar{t}$ region | WW region | $t\bar{t}$ (WW) region | DY (WW) region |
|---|---|---|---|---|---|
| Signal | **14.3** | 0.0 | 6.0 | 0.0 | 0.1 |
| $t\bar{t}$ | 2.6 | **17.0** | 6.2 | 24.7 | 3.2 |
| WW | 5.1 | 0.0 | **11.5** | 0.0 | 4.4 |
| DY | 0.3 | 0.0 | 15.0 | 0.0 | 267 |
| Wt,ZZ,WZ | 0.8 | 0.1 | 1.9 | 0.1 | 7.3 |
| all | 23.1 | 17.1 | 40.6 | 24.8 | 282 |

### 3.2.11 Other backgrounds normalisation

The Drell-Yan background has been normalised to estimate the contamination in the WW region. The same results can be achieved in the signal region. Fig. 3.15 demonstrates that the invariant mass cut 80 GeV/c$^2$ to 100 GeV/c$^2$ defines a clean control region. ZW background can be normalised by requiring one additional lepton in the final state and removing the $\Delta\phi$ and the invariant mass cuts. ZZ background can be normalised by requiring two additional leptons in the final state and removing the $\Delta\phi$ and the invariant mass cuts. They are expected to contribute to the total background by only 3% (DY), 1% (ZW) and 1% (ZZ). For the Wt background it is not easy to define a normalisation region. As this process is expected not to represent a sizable fraction of the total background ($\sim 6\%$), the Monte Carlo prediction will be then directly used, the cross section theoretical uncertainty is estimated to be about 30%

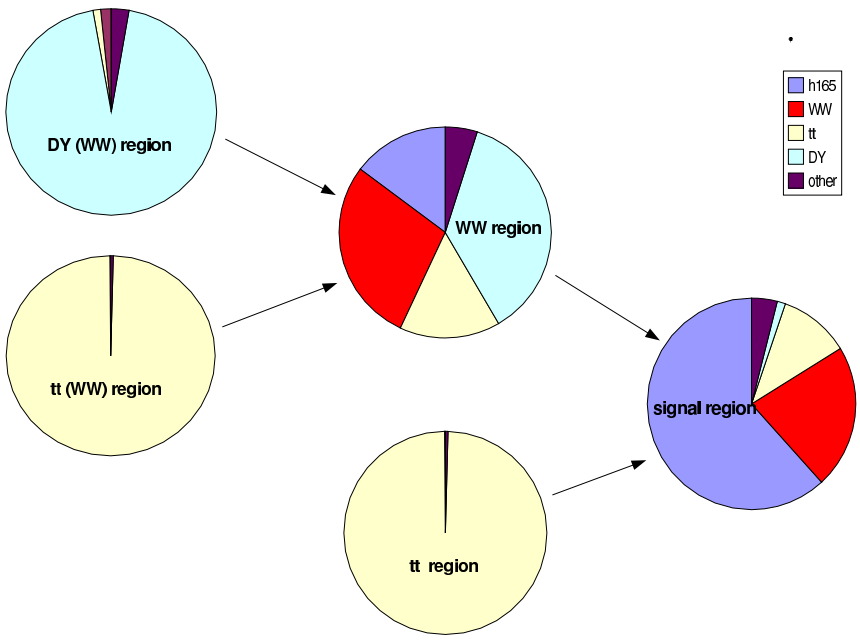


Figure 3.17: Scheme for background normalisation from the data in different phase space regions: the signal region, the $t\bar{t}$ region, the WW region, the DY (WW) region, and the $t\bar{t}$ (WW) region. The arrows indicate the extrapolation of the number of events determined in the corresponding "control region" into the corresponding "target region". Each region is represented by a pie chart that shows the fractions of certain types of events: `h165` is the Higgs signal with $m_h$ = 165 GeV/c$^2$, `WW` is the sum of WW backgrounds, $t\bar{t}$ is the $t\bar{t}$ background, `DY` is the Drell-Yan background, and `other` is the sum of the Wt, ZW and ZZ backgrounds. The number of expected events in each region is reported in Tab. 3.6.

at LO and 10% at NLO [74].

### 3.2.12 Detector misalignment systematics

A study for the misalignment impact on the track reconstruction has been done [85]. In the fist data scenario (100 pb$^{-1}$ - 1 fb$^{-1}$) the muon chamber position uncertainty is expected to be 1 mm and the orientation uncertainty about 0.2 mrad. The tracker position uncertainty is expected to be about 5 $\mu$m for TPE, 10 $\mu$m for TPB, 50 $\mu$m for TEC and TOB, 100 $\mu$m for TIB and 400 $\mu$m for TID. The results from simulation show the muon reconstruction efficiency will be unaffected, while the momentum resolution (for 100 GeV/c tracks) will be reduced from 1-2 % to 4-5%. Under these circumstances, the systematic contribution to the signal and background selection is expected to be negligible with respect to the background normalisation systematics.

### 3.2.13 Signal significance

The signal significance can be obtained using counting or Likelihood methods. Here the counting $S_{cP}$ method (See appendix 1) was used. $S_{cP}$ is the probability, converted in equivalent number of sigmas, to observe at least $N_s + N_b$ events from Poisson distribution with mean $N_b$. The presence of systematic errors influences the significance calculations. The hypothesis is to find the same number of signal and background events predicted by the Monte

Carlo. The systematic errors due to the $t\bar{t}$ and WW background normalisation methods was included. Two options was considered:

1. the signal contamination in the WW control region can be subtracted;
2. the signal contamination in the WW control region must be considered as additional background.

The option 1 was considered to have a comparison with the $H \rightarrow WW \rightarrow 2l2\nu$ analysis [72]. Table 3.7 summaries the total backgrounds and errors for different integrated luminosities. The systematics and statistical errors due to the limited Monte Carlo statistics are included.

Table 3.7: Total background and error for integrated luminosity of 1 and 5 $fb^{-1}$. The two options for the signal contamination in the WW control region were considered.

| Option | Luminosity | Total background | Total error |
|---|---|---|---|
| 1. | 1 $fb^{-1}$ | 8.8 | 3.2 (36%) |
| | 5 $fb^{-1}$ | 44.0 | 8.3 (19%) |
| 2. | 1 $fb^{-1}$ | 11.0 | 3.2 (29%) |
| | 5 $fb^{-1}$ | 55.3 | 8.3 (15%) |

The signal to background ratio as a function of different Higgs masses and the signal significance are shown in Fig. 3.18.

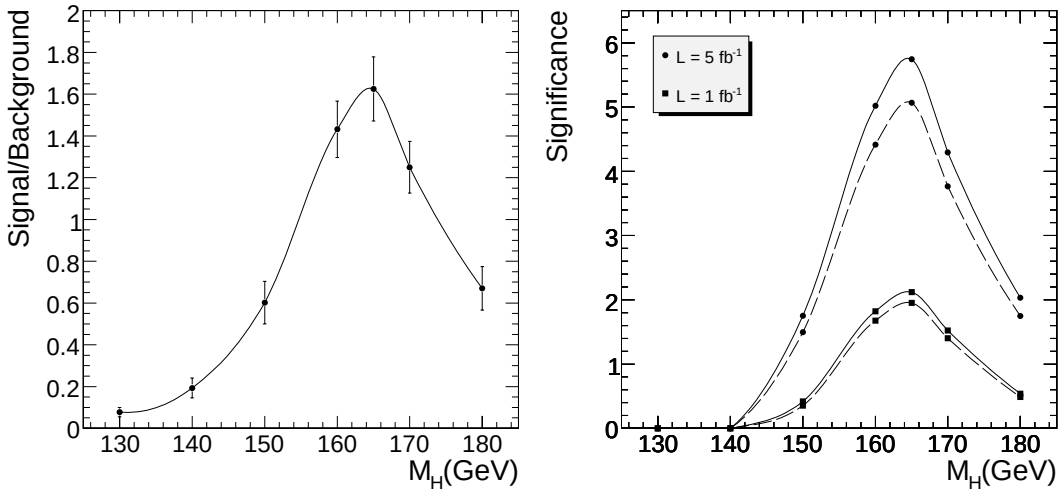


Figure 3.18: Signal to background ratio for the option 1. as a function of different Higgs masses. Error bars are the statistical contribution due to the limited Monte Carlo statistics (left). Significance as a function of different Higgs masses with a luminosity of 1 and 5 $fb^{-1}$, solid line for the option 1., dashed line for the option 2 (right).

### 3.2.14 Conclusions

The possibility to discover the Higgs boson particle through its decay channel into $WW^{(*)} \rightarrow 2\mu 2\nu$ was studied in detail. Particular attention was given to the event selection optimisation, in the determination of the number of background events from the data and the evaluation

of the experimental and theoretical systematical uncertainties. Taking all these effects into account, it was shown that in the Higgs mass range 155-175 GeV/c$^2$ a signal significance bigger than 3 standard deviations can be achieved with 5 fb$^{-1}$ integrated luminosity. On the other hand, with 1 fb$^{-1}$ luminosity only a 2 sigma significance can be achieved even in the most favourable case $m_H \sim 2m_W$, when this final state topology alone is used for the Higgs search.

## 3.3 Benchmark Channel: $Z' \to \mu\mu$

### 3.3.1 Introduction

Additional heavy neutral gauge bosons (Z′) are predicted in many superstring-inspired [86, 87] and grand unified theories (GUTs) [88], as well as in dynamical symmetry breaking [89] and "little Higgs" [90] models. There are no reliable theoretical predictions, however, of the Z′ mass scale. Current lower limits on the Z′ mass are (depending on the model) of the order of 600–900 GeV/c$^2$ [54]. The mass region up to about 1 TeV/c$^2$ is expected to be explored at Run II at the Tevatron [91, 92]. The LHC offers the opportunity to search for Z′ bosons in a mass range significantly larger than 1 TeV/c$^2$.

Observability of the Z′ $\to \mu^+\mu^-$ channel in CMS is discussed in Sections 3.3.2–3.3.4. Since narrow graviton resonances such as those in Randall-Sundrum models [93] can also decay to lepton pairs (Section 14.3.1), much of the discussion in these sections is also applicable to them. If a new resonance is discovered, the characterisation of its spin and couplings will proceed via the traditional methods of measuring production and decay probabilities and distributions. For example, the two-photon decay should be observable for a graviton and not for a Z′, as discussed in Section 14.6. The measurement of forward-backward asymmetries of leptonic decay products, both at the resonance peak and off the peak, yields information on parity-violating couplings and hence can help distinguish among different Z′ models (Section 3.3.5). Angular distributions of the decay products can also be used for spin discrimination (Section 3.3.6).

### 3.3.2 Signal and background processes

#### 3.3.2.1 Signal Z′ $\to \mu^+\mu^-$

Signal and background samples were generated with PYTHIA [68] version 6.227 (with photon emission off incoming or outgoing quarks and leptons switched on) and the CTEQ6L set of parton distribution functions [12] from LHAPDF [94] version 4.1.1.

From a large variety of Z′ bosons described in the literature, we consider six which are frequently discussed, and whose properties are representative of a broad class of extra gauge bosons:

- $Z_{SSM}$ within the Sequential Standard Model (SSM), which has the same couplings as the Standard Model $Z^0$; it is available in PYTHIA [24].
- $Z_\psi$, $Z_\eta$ and $Z_\chi$, arising in $E_6$ and SO(10) GUT groups. Couplings to quarks and leptons were obtained from Refs. [95, 96].
- $Z_{LRM}$ and $Z_{ALRM}$, arising in the framework of the so-called "left-right" [97] and "alternative left-right" [91, 92] models. Their couplings were obtained from Ref. [91, 92], with the choice of $g_R = g_L$.

The generation of signal events with PYTHIA includes the full $\gamma^*/Z^0/Z'$ interference structure. We assume that Z′ bosons decay only to three ordinary families of quarks and leptons and that no exotic decay channels are open. Properties for these models are in Table 3.8. The cross sections are shown at leading order (LO), as predicted by PYTHIA. We scale them by a constant $K$ factor of 1.35, see Appendix C, in order to take into account the next-to-next-to-leading order (NNLO) QCD corrections. Electroweak higher-order corrections are not yet accounted for (see discussion in Section 3.3.4.4.1).

Table 3.8: Summary of expected properties of Z′ bosons for six studied models. For each model, the first column shows the ratio of the total Z′ decay width $\Gamma$ to its mass $M$, the second column shows the dimuon branching ratio Br. The three middle columns, labelled $\sigma^{\mathrm{LO}} \cdot \mathrm{Br}$, give the product of the pure-Z′ leading-order production cross section and the branching ratio for three studied Z′ masses; the last three columns give $\sigma^{\mathrm{LO}} \cdot \mathrm{Br}$ obtained when the full $\gamma^*/Z^0/Z'$ interference structure is included. The numbers quoted are for the mass intervals above 400 GeV/c$^2$ for $M = 1$ TeV/c$^2$, above 1.5 TeV/c$^2$ for $M = 3$ TeV/c$^2$, and above 3 TeV/c$^2$ for $M = 5$ TeV/c$^2$. The values of $\sigma \cdot \mathrm{Br}$ in the three middle columns correspond to Z′-only samples not used in our study; the values in the last three columns refer to the full-interference samples that we did use.

| Model | $\Gamma/M$ % | $Z' \to \mu^+\mu^-$ BR in % | $\sigma^{\mathrm{LO}} \cdot \mathrm{Br}$, fb (PYTHIA) | | | $\sigma^{\mathrm{LO}} \cdot \mathrm{Br}$, full interference, fb (PYTHIA) | | |
|---|---|---|---|---|---|---|---|---|
| | | | 1 TeV/c$^2$ | 3 TeV/c$^2$ | 5 TeV/c$^2$ | 1 TeV/c$^2$ | 3 TeV/c$^2$ | 5 TeV/c$^2$ |
| $Z_{\mathrm{SSM}}$ | 3.1 | 3.0 | 480 | 1.9 | 0.034 | 610 | 2.8 | 0.050 |
| $Z_\psi$ | 0.6 | 4.0 | 130 | 0.5 | 0.009 | 340 | 1.7 | 0.032 |
| $Z_\eta$ | 0.7 | 3.4 | 150 | 0.6 | 0.011 | 370 | 1.8 | 0.035 |
| $Z_\chi$ | 1.3 | 5.7 | 280 | 1.0 | 0.014 | 500 | 2.2 | 0.038 |
| $Z_{\mathrm{LRM}}$ | 2.2 | 2.3 | 310 | 1.2 | 0.020 | 500 | 2.3 | 0.040 |
| $Z_{\mathrm{ALRM}}$ | 1.6 | 8.6 | 580 | 2.6 | 0.051 | 740 | 3.7 | 0.077 |

#### 3.3.2.2 Background from Drell-Yan production and other processes

The dominant (and irreducible) background to $\mathrm{pp} \to Z' \to \mu^+\mu^-$ is the Drell-Yan production of muon pairs, $\mathrm{pp} \to \gamma/Z^0 \to \mu^+\mu^-$. The Drell-Yan cross section in PYTHIA was scaled by the same $K$ factor of 1.35, see Appendix C, to get an agreement with the NNLO QCD calculations.

The overall contribution from ZZ, ZW, WW, and $t\bar{t}$ was found to be at the level of only a few percent of the Drell-Yan background and can be further suppressed by signal-selection criteria with almost no reduction in signal efficiency; we neglect this contribution. A few other potential background sources (like cosmics, jet-jet, W-jet, $b\bar{b}$, hadron punchthroughs, and poorly measured $Z^0 \to \mu^+\mu^-$ events) have not been studied yet, but their contribution is expected to be small.

#### 3.3.2.3 Simulation and reconstruction

The detector response was simulated with the detailed CMS detector simulation and reconstruction software, including pile-up events. Misalignments of the tracker and of the muon system expected at the initial and at the well-advanced stages of the data taking have been

taken into account by using two misalignment scenarios developed in the framework of the CMS reconstruction, referred to as the "first data" and the "long term" scenarios [85]:

- The "first data" scenario gives an estimate of the alignment achieved with an integrated luminosity of about 0.1 $\text{fb}^{-1}$ and corresponds to the situation when the pixel detector is aligned with tracks and the first information from the Laser Alignment System (LAS) is available for the muon detectors.
- The "long term" scenario describes the expected residual alignment uncertainties once the performance of the LAS reaches its design level and the alignment with tracks is done in all tracking detectors. The current estimate is that this can be achieved with an integrated luminosity of about 1 $\text{fb}^{-1}$.

As a result, for each of the Z′ models above, several sets of simulated samples corresponding to different possible combinations of luminosities and misalignment scenarios were produced at each of three mass values of 1, 3, and 5 $\text{TeV/c}^2$. Since the Drell-Yan cross section falls rapidly with the mass of the muon pair, Drell-Yan background was generated in six mass intervals (with lower mass bounds of 0.2, 0.4, 1, 1.5, 2, and 3 $\text{TeV/c}^2$), again for different combinations of luminosities and misalignment scenarios.

### 3.3.3 Event selection

For $\mu^+\mu^-$ invariant mass between 1 $\text{TeV/c}^2$ and 5 $\text{TeV/c}^2$, the fraction of Drell-Yan events with both muons within the full geometrical acceptance of the muon system ($|\eta| < 2.4$) increases from about 80% at 1 $\text{TeV/c}^2$ to almost 95% at very high masses. The acceptance of $Z' \to \mu^+\mu^-$ events is very similar.

We require that the event pass the logical OR of single-muon and dimuon triggers, both Level-1 and HLT. We use the default ORCA implementations of low-luminosity and high-luminosity muon trigger algorithms described in Refs. [7, 75], with the exception of the HLT calorimeter isolation criterion requiring that the weighted sum of energy deposits in ECAL and HCAL in a cone around the muon direction be below a pre-defined threshold. Its current implementation leads to significant efficiency losses for *isolated* high-$p_{\mathrm{T}}$ muons (since they are often accompanied by electromagnetic showers); we do not apply HLT calorimeter isolation in this study (tracker isolation is applied). An increase in the trigger rate in the absence of calorimeter isolation should be mitigated by higher $p_{\mathrm{T}}$ thresholds; we have checked that raising the $p_{\mathrm{T}}$ thresholds of the single-muon HLT by 10–20 GeV with respect to their nominal values changes trigger efficiency for our signals by a negligible amount. For the Z′ models that we study (as well as for the Drell-Yan background), the combined Level-1/HLT trigger efficiency is about 98% at 1 $\text{TeV/c}^2$ and decreases with the Z′ mass down to about 95% at 5 $\text{TeV/c}^2$. At high luminosity, the trigger efficiency is 95% at 1 $\text{TeV/c}^2$ and 93% at 5 $\text{TeV/c}^2$. These efficiencies are relative to having at least one muon inside the geometrical acceptance of the muon trigger ($|\eta| < 2.1$) and both muons from the Z′ decay inside the full acceptance of the muon system. No dependence of trigger efficiency on tracker and muon misalignment has been observed, in agreement with the results reported in Ref. [98].

We require that at least two muons of opposite sign charge be reconstructed offline. Detailed description of offline muon reconstruction can be found in Ref. [7]. For each muon candidate, we examine the results of fits to two subsets of hits associated to this candidate: 1) excluding all muon hits except for those in the innermost muon station, and 2) excluding hits in muon chambers appearing to contain electromagnetic showers. Optimal performance for high-$p_{\mathrm{T}}$

muons is achieved by choosing the best fit on a track-by-track basis using goodness-of-fit variables. The fraction of Z′ events with an opposite-sign dimuon reconstructed offline is about 97% at 1 TeV/c$^2$ for both the "first data" and the "long term" misalignment scenarios, and decreases slightly with the Z′ mass, to about 95% at 5 TeV/c$^2$ for the "long term" misalignment scenario. The efficiencies quoted are calculated relative to the number of events accepted by the trigger and with both muons from the Z′ decay within the full geometrical acceptance of the muon system.

The overall efficiency – including acceptance, trigger and offline reconstruction – for $Z' \rightarrow \mu^+\mu^-$ events with a mass between 1 and 5 TeV/c$^2$ lies in the range of 77–85% at low luminosity, and of 75–83% at high luminosity.

### 3.3.4 Signal observability

The search for a new resonance is performed with an unbinned maximum likelihood fit to the $\mu^+\mu^-$ invariant mass spectrum over a range which includes Drell-Yan continuum as well as a possible peak. The fit takes as input the presumed signal and background shapes, and determines the best-fit background normalisation. More details are in Refs. [99, 100].

#### 3.3.4.1 Mass spectra and fitting procedure

Prior to the calculation of the invariant mass of an opposite-sign muon pair, $\sqrt{s}$, a search for photon candidates in a cone with a radius of $\Delta R = \sqrt{(\Delta\phi)^2 + (\Delta\eta)^2} < 0.1$ around the trajectory of each muon is performed, and the 4-momentum of the photon candidate with the smallest $\Delta R$ in the cone is added to the 4-momentum of the muon. This procedure recovers some of the energy lost by the muon via final state radiation and radiative processes in the detector, thus improving the invariant mass resolution.

The resolution for $\sqrt{s}$ depends strongly on the misalignment scenario, and weakly on the amount of pile-up. If the "long term" misalignment scenario for the tracker and the muon chambers is considered, the sigma of the Gaussian fit to the mass resolution curves varies from 4.2% at 1 TeV/c$^2$ to 9.0% at 5 TeV/c$^2$; the RMS truncated at $\pm 30\%$ is $\sim 6\%$ at 1 TeV/c$^2$ and $\sim 10\%$ at 5 TeV/c$^2$. The corresponding numbers for the "first data" misalignment scenario at 1 TeV/c$^2$ are $\sigma$ = 12.5% and RMS $\sim 12\%$. The bias in the mass resolution does not exceed 1% for the "long term" scenario at all masses considered and for the "first data" scenario at 1 TeV/c$^2$.

An example of the $\sqrt{s}$ spectra showing 1 TeV/c$^2$ $Z_\eta$ signal and Drell-Yan background is in Figure 3.19. The left-hand plot shows generated mass spectra (100% efficiency with no detector- and reconstruction-related effects); it can be compared to the right-hand plot for fully-reconstructed events using the "first data" misalignment scenario. Signal peak is clearly visible in spite of the poor mass resolution.

The mass spectra in Figure 3.19 are obtained by re-scaling the simulated spectra with large statistics down to a modest number of events characteristic for the regime close to the discovery limit; the statistical fluctuations are thus not to scale. In what follows, we use ensembles of Monte Carlo pseudo-experiments selected from available large-statistics samples. The number of events in each experiment, $N_{\rm evt}$, fluctuates according to a Poisson distribution with a mean of $\sigma \cdot {\rm Br} \cdot \int \mathcal{L} dt \cdot \varepsilon$, where $\int \mathcal{L} dt$ is the integrated luminosity and $\varepsilon$ is the combined trigger and reconstruction efficiency.

In order to test for the existence of a resonance and to measure its parameters if it is found

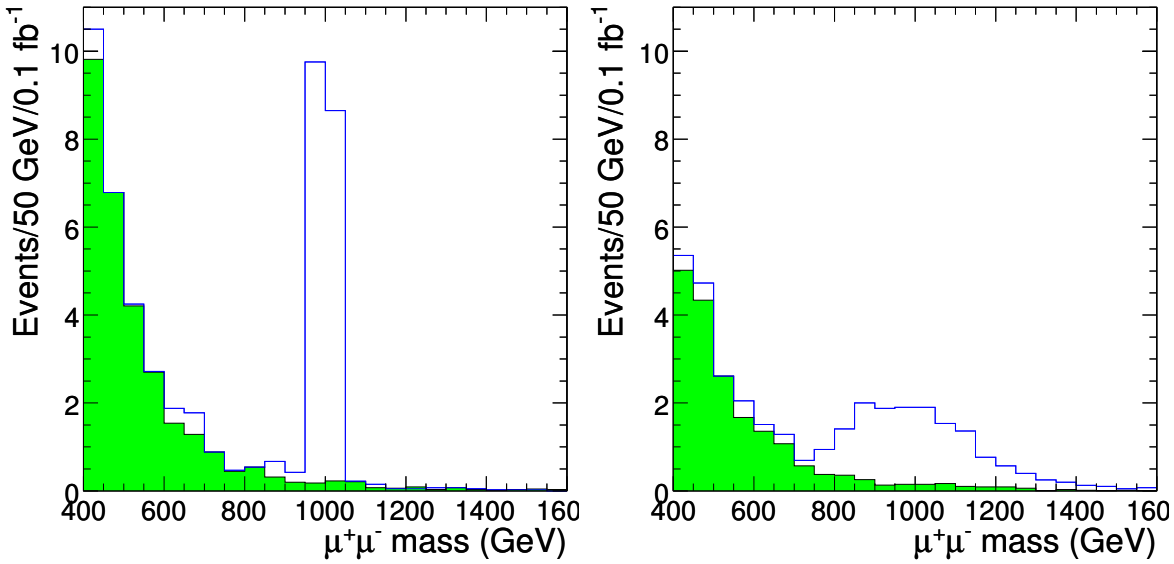


Figure 3.19: Histograms of the $\mu^+\mu^-$ invariant mass for 1 TeV/c$^2$ $Z_\eta$ plus background (open histogram) and for background only (shaded histogram), at the event-generator level (left) and for events selected by the Level-1/HLT triggers and reconstructed assuming the "first data" misalignment scenario (right). The number of events per bin is normalised to an integrated luminosity of 0.1 fb$^{-1}$.

to exist, an unbinned maximum likelihood fit of the $\sqrt{s}$ values in each MC experiment is appropriate. One can imagine that, in the initial data analysis, one is confident about the background shape but not the absolute normalisation. In this case, data can be fit with a sum of signal and background shapes, presumed known, with the signal fraction as a free parameter. In the presence of a signal, one can fix or let vary the mass and the width as well. Thus, as a model of the probability density function (pdf), $p$, of the parent population of the observed mass spectra, we use

$$p\,(\sqrt{s}; f_s, m_0, \Gamma) = f_s \cdot p_s\,(\sqrt{s}; m_0, \Gamma) + (1 - f_s) \cdot p_b\,(\sqrt{s}). \tag{3.19}$$

Here

- $p_s$, the pdf of the signal, is a convolution of a Breit-Wigner signal shape with a Gaussian accounting for mass resolution smearing. The convolution includes the dependence of the mass resolution on $\sqrt{s}$, but the radiative tail of the signal is not yet accounted for.
- $p_b$, the pdf of the background, is modelled as an exponential, $\exp(-k \cdot \sqrt{s}^{0.3})$, with the parameter $k$ determined from fits to Drell-Yan events. This pdf, with the value of $k$ of 2.0, gives a good description of the background shape in the whole mass region between 400 and 5000 GeV/c$^2$.

There are three free parameters in the fit: the signal fraction $f_s = N_s/(N_s + N_b)$, the position of the mass peak $m_0$, and the full width at half maximum (FWHM), $\Gamma$, of the signal. The shape of the background distribution is fixed, while its level is determined by the fit: $f_s$ is a free parameter. Therefore, the fit explores the difference *in shape* between the signal and the background, and is not sensitive to uncertainties in the expected signal and background levels.

Table 3.9: Average values of the likelihood-ratio significance estimator $S_{\mathcal{L}}$ for six different Z′ models, at three signal mass points and for a few representative values of an integrated luminosity. The uncertainties shown are statistical only.

| Mass | 1 TeV/c$^2$ | 3 TeV/c$^2$ | 5 TeV/c$^2$ |
|---|---|---|---|
| $\int \mathcal{L}dt$ | 0.1 fb$^{-1}$ | 10 fb$^{-1}$ | 300 fb$^{-1}$ |
| $Z_{SSM}$ | $12.4 \pm 0.2$ | $10.1 \pm 0.2$ | $5.8 \pm 0.1$ |
| $Z_{\psi}$ | $5.1 \pm 0.2$ | $4.4 \pm 0.1$ | $2.4 \pm 0.2$ |
| $Z_{\eta}$ | $5.5 \pm 0.2$ | $5.1 \pm 0.1$ | $2.9 \pm 0.1$ |
| $Z_{\chi}$ | $9.1 \pm 0.2$ | $6.7 \pm 0.2$ | $3.2 \pm 0.1$ |
| $Z_{LRM}$ | $9.0 \pm 0.2$ | $7.4 \pm 0.2$ | $4.1 \pm 0.1$ |
| $Z_{ALRM}$ | $13.3 \pm 0.3$ | $11.8 \pm 0.2$ | $7.7 \pm 0.2$ |

The background shape is currently determined from fits to large-statistics background-only simulated distributions in the full mass region of interest, including the region under the signal peak. In the real experiment, the shape will likely have to be extracted from the data in signal-free regions. The accuracy of predicting the background shape is an important contribution to the systematic uncertainty of the analysis and is discussed in Section 3.3.4.4.3.

Ref. [99] contains examples of results of fits to Monte Carlo small-event samples. With even the small number of events needed to give evidence of a resonance, the mass is determined fairly well, with a precision of 4–8% depending on the resonance mass and alignment uncertainties. However, for the narrow resonances under study, typically little information can be obtained about the width.

#### 3.3.4.2 Significance estimator

We follow closely the approach of Ref. [101], which is based on the theorem of S.S. Wilks [102]. The test statistic is the likelihood-ratio estimator $S_{\mathcal{L}}$:

$$S_{\mathcal{L}} = \sqrt{2 \ln \left( \mathcal{L}_{s+b} / \mathcal{L}_b \right)}, \tag{3.20}$$

where $\mathcal{L}_{s+b}$ is the maximum likelihood value obtained in the full signal-plus-background fit, and $\mathcal{L}_b$ is the maximum likelihood from the background-only fit. Studies show [99] that in the small-statistics low-background regime characteristic of a Z′ search, the asymptotic conditions of Wilks's theorem [102] are satisfied well enough and $S_{\mathcal{L}}$ is the number of Gaussian-equivalent standard deviations a measurement lies from the value predicted by a background-only (null) hypothesis. This requires fixing both $m_0$ and $\Gamma$ in the fits using the pdf of Eq. (3.19).

We follow a common convention in using the (arbitrary, but useful for comparison) specification that $S > 5$ is necessary to establish a discovery. This $S$ refers to the local excess without accounting for the degree of freedom due to the unknown mass; how one might de-rate $S$ in a time-dependent way in this context as data comes in will be the subject of a future study.

#### 3.3.4.3 Discovery potential in $Z' \to \mu^+\mu^-$ channel

Table 3.9 gives a summary of the signal significance expected for different Z′ models, masses and integrated luminosities. The numbers shown are for the "first data" misalignment scenario and low luminosity parameters for $\int \mathcal{L}dt = 0.1\,\text{fb}^{-1}$, the "long term" misalignment

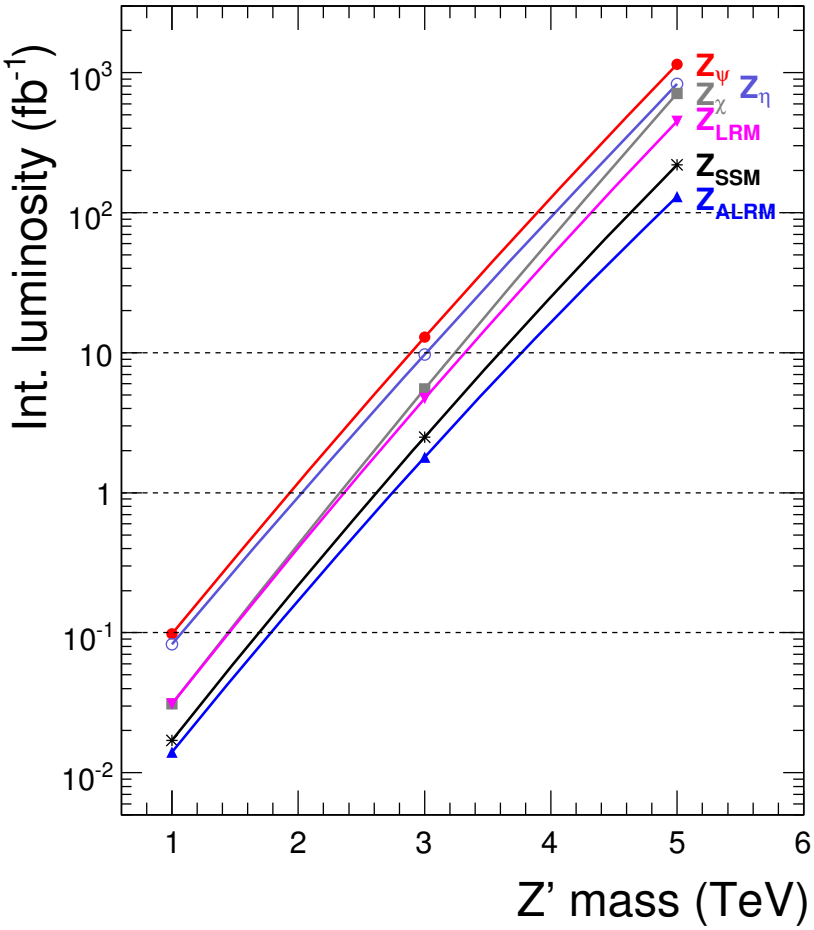


Figure 3.20: Integrated luminosity needed to reach $5\sigma$ significance ($S_{\mathcal{L}} = 5$) as a function of Z′ mass for (top to bottom) $Z_\psi$, $Z_\eta$, $Z_\chi$, $Z_{LRM}$, $Z_{SSM}$ and $Z_{ALRM}$. Symbols indicate fully-simulated mass-luminosity points, lines are the results of interpolations between the points.

scenario and low luminosity parameters for 10 fb$^{-1}$, and the "long term" misalignment scenario and high luminosity parameters for 300 fb$^{-1}$. $S_{\mathcal{L}}$ scales as expected with the square root of $\int \mathcal{L} dt$.

We use the same combinations of luminosities and misalignment scenarios to calculate the integrated luminosity needed to reach $5\sigma$ significance. The results for various Z′ models are shown in Figure 3.20 as a function of Z′ mass. One can see that

- A very low integrated luminosity, less than 0.1 fb$^{-1}$, and non-optimal alignment of the tracker and the muon detectors should be sufficient to discover Z′ bosons at 1 TeV/c$^2$, a mass value which will likely be above the Tevatron reach. One would need about 50% less data to reach the same signal significance if the optimal alignment is achieved.
- An integrated luminosity of 10 fb$^{-1}$ is sufficient to reach $5\sigma$ significance at 3 TeV/c$^2$ for most (but not all) of the Z′ models considered if the optimal alignment is available: depending on the model, the mass reach is in the range between 2.9 and 3.8 TeV/c$^2$.

- An integrated luminosity of 100 fb$^{-1}$ does not allow one to obtain $5\sigma$ significance at 5 TeV/c$^2$ with only the Z′ $\rightarrow \mu^+\mu^-$ channel for any of the models considered: the corresponding mass reach lies in the region between 3.9 and 4.9 TeV/c$^2$.

These estimates of signal significance do not incorporate systematic uncertainties, which we discuss in the next section.

#### 3.3.4.4 Systematic uncertainties

The main sources of systematic uncertainties are expected to be a) theoretical uncertainties (parton distributions, higher-order corrections, etc.), b) uncertainties arising from an imperfect knowledge of the detector (alignment, calibration, magnetic field), and c) uncertainties in the fitting procedure (background shape, functional forms of pdf's, mass resolution, etc.).

**3.3.4.4.1 Theoretical uncertainties** Our current estimates of the Z′ mass reach depend on the accuracy of the modelling of the Standard Model processes and of the Z′ boson production. The following sources of theoretical uncertainties have been studied:

- **Higher-order QCD corrections.** We use a constant $K_{\rm QCD}^{\rm NNLO}$ factor of 1.35 to rescale PYTHIA cross sections for Drell-Yan and Z′ bosons to NNLO QCD predictions. This is an approximation, since such a reweight does not take into account variations of the ratio of NNLO and LO cross sections with the invariant mass and other observables, such as rapidity and $p_{\rm T}$. It is shown in Appendix C that the variations of the $K_{\rm QCD}^{\rm NNLO}$ factor with the mass in the mass interval between 500 GeV/c$^2$ and 5 TeV/c$^2$ is in the range of $\Delta K_{\rm QCD} = \pm 0.05$; the dependence on other observables and the ensuing impact on acceptance, efficiency, etc. remains to be studied. Since $K$ is expected to be nearly identical for the signal and dominant background, the effect of changes in $K$ from the nominal value $K_0 = 1.35$ is to scale the expected significance by $\sqrt{K/K_0}$.
- **Higher-order electroweak corrections.** Only preliminary estimates of electroweak next-to-leading order corrections exist for the LHC and $\sqrt{s} > 1$ TeV/c$^2$ [103, 104]. Currently, we use $K_{\rm EW} = 1$ for the central values of signal and background cross-sections, and assign an uncertainty of $\Delta K_{\rm EW} = \pm 0.10$ based on discussions in Refs. [103, 104].
- **Parton distribution functions (PDFs).** We use the CTEQ6.1M eigenvector PDF sets [12] and the "master" equations in Ref. [105] to evaluate the uncertainties characterising current knowledge of the parton distributions. The effect on the total cross section $\sigma$ was found to be similar for the Drell-Yan background and for the studied Z′ models at any given mass, with uncertainties lying in the range of $\frac{\Delta\sigma}{\sigma} = ^{-7\%}_{+4\%}$ at $\sqrt{s}$ = 1 TeV/c$^2$, rising to $^{-10\%}_{+12\%}$ at $\sqrt{s}$ = 3 TeV/c$^2$, and reaching as much as $^{-20\%}_{+30\%}$ at $\sqrt{s}$ = 5 TeV/c$^2$. The effect on other observables and on the acceptance has not been studied yet, but is expected to be small.
- **Hard process scale.** The dependence of the observables on the choice for renormalisation and factorisation $Q^2$ scales, $\mu_R$ and $\mu_F$, is unphysical and is commonly taken as a rough estimate of the uncertainty due to unaccounted higher orders in QCD calculations. The study of the sensitivity of the Drell-Yan cross section to the choice for the QCD scale is described in Appendix C. Both $\mu_F$ and $\mu_R$ were varied in the range of $\sqrt{s}/2 < \mu < 2\sqrt{s}$ around the default choice of $\mu = \sqrt{s}$, and

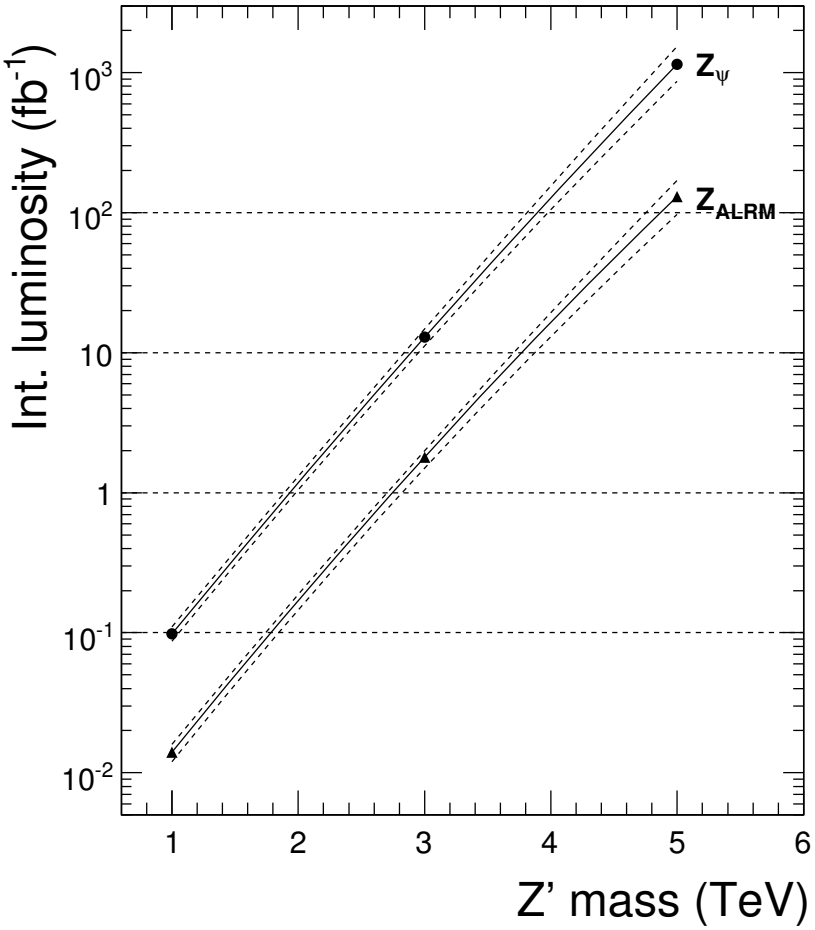


Figure 3.21: Integrated luminosity needed to reach $5\sigma$ significance ($S_{\mathcal{L}} = 5$) as a function of Z′ mass for $Z_\psi$ and $Z_{\mathrm{ALRM}}$ models. Solid lines show the best estimates, dashed lines indicate boundaries of the band corresponding to the predictions with $\pm 1\sigma$ theoretical uncertainty.

the mass-dependent variations of the cross section obtained. At NNLO, they are smaller than $\pm 1\%$ at 1 TeV/c$^2$, but as large as $-25\%$ (for $\mu = 2\sqrt{s}$) and $+5\%$ (for $\mu = \sqrt{s}/2$) at 5 TeV/c$^2$. We use the NNLO estimates given in Appendix C for both the Drell-Yan and the Z′ bosons.

Since our analysis relies only on the background shape and not on any assumptions about background normalisation, the uncertainties in signal and background cross sections described in this section will not have any direct impact on the calculation of significance once a data set is in hand. They do effect, however, estimates of the Z′ mass reach based on Monte Carlo predictions for the signal and the background. We combine them in quadrature, and use the obtained mass-dependent band as $1\sigma$ uncertainty in the expected number of signal and background events. This band is then translated into $1\sigma$ uncertainty in the prediction of the mean integrated luminosity needed to reach $5\sigma$ significance for any given Z′ model. This uncertainty, and the best estimates of the luminosity, is shown in Figure 3.21 for the models with the smallest and the largest values of $\sigma \cdot \mathrm{Br}$ among the models studied, $Z_\psi$ and $Z_{\mathrm{ALRM}}$.

**3.3.4.4.2 Uncertainties in the detector performance** The key element in the performance of high-$p_{\mathrm{T}}$ muon reconstruction and, therefore, for the Z′ mass reach is the alignment

of the tracker and the muon system. Unlike the muons in the region of low and moderate $p_{\mathrm{T}}$ values, where the influence of the tracker alignment is predominant, both the tracker alignment and the muon system alignment play an important role for the muons at TeV scale. We take them into account by using the two realistic misalignment scenarios developed in the CMS reconstruction, the "first data" and the "long term". These scenarios, however, are only based on the current best estimates (and sometimes guesses) of expected alignment uncertainties and will be refined as better estimates from alignment studies become available. Therefore, they have intrinsic uncertainties, which at the moment cannot be evaluated. As discussed above and in Ref. [98], neither the trigger efficiency nor the offline reconstruction efficiency for high-$p_{\mathrm{T}}$ muons is affected by the misalignment even in the worst-case scenario once the alignment position uncertainties are used in reconstruction algorithms [85]. So uncertainties in alignment translate mainly into uncertainties in the invariant mass resolution. We show below that even sizable variations in the width of the mass resolution have only a small impact on the Z′ mass reach.

Another potentially important source of systematic uncertainties is the uncertainty in the calibration precision of the muon chambers. The impact of uncertainties in the calibration of the Drift Tube chambers on the Z′ mass reach has been studied by 1) changing the $t_0$ offsets for all chambers by $\pm 2$ ns, and 2) scaling drift velocity (changing time-to-distance relationship) by $\pm 3\%$. These variations represent conservative upper bounds on corresponding effects [106]. The effect of changing $t_0$ offset was found to be negligible for Z′ samples at all studied mass values and for both misalignment scenarios considered. The scaling of drift velocity has a negligible impact for the "first data" misalignment scenario with its rather poor mass resolution, but results in an increase of 5–10% in the width of the mass resolution for the "long term" scenario (no change in trigger and dimuon reconstruction efficiencies). This translates into a negligible effect in the Z′ mass reach. Uncertainties in the calibration of the Cathode Strip Chambers are less critical and hence are expected to have a negligible impact on the Z′ detection as well.

The effect of uncertainties in the knowledge of the magnetic field remains to be studied.

**3.3.4.4.3 Uncertainties in background shape and mass resolution** Many experimental uncertainties have a negligible or small impact on the results of our studies because the proposed analysis method is not sensitive to uncertainties in the predicted levels of signal and background processes. For example, only the mass dependence of the uncertainty in the muon reconstruction efficiency needs to be taken into account, not the absolute uncertainty. The same is true for the trigger efficiency and for the uncertainty in the $\sqrt{s}$ scale. Among those uncertainties that do not cancel out, two seem to be particularly important: the uncertainty in the background shape, and the uncertainty in the mass resolution.

As described above, the background shape is currently determined from fits to background distributions predicted by the Monte Carlo simulation. In the analysis of real data, this MC-based shape will be compared with (and perhaps tuned to) the background shape in the region of low masses where one has high statistics of background events. The issue is then the reliability of the extrapolation from the steeply falling spectrum into the candidate signal region. This will have to be studied in detail once the real data starts to be available. What is interesting to explore at this stage of analysis is how rapidly the significance deteriorates as the ratio of background events in the high-statistics normalisation region to background events in the candidate signal region is wrongly predicted by the MC-motivated background

shape. To study this, we multiply our background pdf ($p_b$ in Eq. (3.19)) by a function which is unity in the high-statistics background-only region and smoothly transitions to a tunable value, $f$, under the candidate mass peak. Values of integrated luminosity were chosen to correspond to $5\sigma$ significance for each model at $f = 1$. For $f = 2$ (assuming twice as much background in the signal region as there really is), $5\sigma$ becomes $4.2\sigma$ for $\mathrm{Z_{ALRM}}$ and is about $3.7\sigma$ for $\mathrm{Z_\psi}$. For $f$ around 1.1 or 1.2, the change in $S$ is of the order of a few per cent.

Sensitivity of the Z′ mass reach to uncertainties in the invariant mass resolution has been studied by applying extra Gaussian smearing to the reconstructed values of $\sqrt{s}$ of both the signal and background events and comparing the signal significance obtained with modified $\sqrt{s}$ values to that calculated with the nominal $\sqrt{s}$ values. We found that an increase of 10% in the mass resolution width, $\sigma_M$, reduces the signal significance by less than 2% at the values of $S_\mathcal{L}$ close to 5; 20% worse resolution gives 5% or less smaller $S_\mathcal{L}$. The effect is not very big, indicating that an approximate knowledge of $\sigma_M$ should suffice. (This exercise does not check, however, the effect of extreme tails of the mass resolution being bigger than expected, which could lead to a background shape (and amount) different from that obtained from the simulation.) The knowledge of $\sigma_M$ as a function of $\sqrt{s}$ is also used in the pdf of the signal in Eq. (3.19), where it defines the width of a Gaussian accounting for resolution smearing of the signal shape. This does not need to be very precise either: assuming resolution 20% better that it really is reduces $S_\mathcal{L}$ by less than 1%.

### 3.3.5 Distinguishing among $\mathrm{Z}'$ models

The forward-backward asymmetry, $A_{\mathrm{FB}}$, of the leptonic decay products provides information on parity-violating couplings, on and off resonance, as discussed for example in Refs. [95, 107].

The forward-backward asymmetry for $q\bar{q} \to \mu^+\mu^-$ interactions is defined as (e.g., Refs. [108, 109])

$$A_{\mathrm{FB}} = \frac{\sigma_F - \sigma_B}{\sigma_F + \sigma_B}, \tag{3.21}$$

where

$$\sigma_F \equiv \int_0^1 \frac{d\sigma(q\bar{q} \to \mu^+\mu^-)}{d\cos\theta^*} d\cos\theta^*, \quad \sigma_B \equiv \int_{-1}^0 \frac{d\sigma(q\bar{q} \to \mu^+\mu^-)}{d\cos\theta^*} d\cos\theta^*, \tag{3.22}$$

and where $\theta^*$ is the angle in the dimuon centre-of-mass (CM) reference frame between the negative muon and the incident quark. For spin-1 $\gamma^*/\mathrm{Z}^0/\mathrm{Z}'$ propagators, the probability density function $P(\cos\theta^*)$ is most generally of the form

$$P(\cos\theta^*; A_{\mathrm{FB}}, b) = \frac{3}{2(3+b)}(1 + b\cos^2\theta^*) + A_{\mathrm{FB}}\cos\theta^*. \tag{3.23}$$

Although $b = 1$ from general considerations, in the fits described here $b$ is typically left as a free parameter. In Ref. [96], Rosner expresses $A_{\mathrm{FB}}$ for $f\overline{f} \to \gamma^*/\mathrm{Z}^0/\mathrm{Z}' \to \mu^+\mu^-$ events in terms of the left- and right-handed couplings of the photon, $Z^0$, and Z′ to $u$ quarks, $d$ quarks, and charged leptons. More details, including the couplings for the models studied, are given in Ref. [110].

For CM energies well above the $Z^0$ peak, the Drell-Yan background has a characteristic $A_{\mathrm{FB}}$ of about 0.6 [108], and provides a useful starting point.

#### 3.3.5.1 Uncertainty in the sign of $\cos\theta^*$ in pp collisions

In proton-proton interactions, the quark direction is ambiguous experimentally since a quark can originate with equal probability from either proton, and the sign of $\cos\theta^*$ is not directly measurable. We follow Ref. [111] and infer the sign of $\cos\theta^*$ by assuming that the longitudinal motion of the dimuon system is in the direction of the proton contributing the annihilating quark, since a quark in a proton typically carries a larger momentum fraction $x$ than does an anti-quark. We refer to the inference of the wrong sign of $\cos\theta^*$ as "mistagging" the sign. If not accounted for, the mistagged events, particularly at low $y$, reduce ("dilute") the apparent value of $A_{\rm FB}$. Some authors deal with this problem by removing events below a chosen $y$ threshold [111], or by examining $A_{\rm FB}$ in bins of $y$ [112]; in Ref. [110], an approached is described which assigns the probability of a mistag on an event-by-event basis, thus using all events in a given sample. As knowledge of the mistagging probability depends on the Parton Distribution Functions, the effect of uncertainties in PDFs must be evaluated, and will be the subject of future work.

#### 3.3.5.2 Other uncertainties

The transverse momentum $p_{\rm T}$ of the annihilating quark and/or anti-quark provides another source of uncertainty in the measurement of $\cos\theta^*$, since the observable quantity is the vector sum of these transverse momenta. We use the Collins-Soper reference frame [113], in which angles are measured with respect to the axis that bisects the target and beam axes in the dimuon CM frame, to minimise the effect of $p_{\rm T}$ on the measurement of $\cos\theta^*$, and let $\theta^*_{\rm CS}$ denote the polar angle of the $\mu^-$ in this frame.

As described in Ref. [110], the effect of detector acceptance, combined with high mistag probability for events near $y = 0$, means that events lying near the edges of acceptance carry the largest information for the $A_{\rm FB}$ measurement. Hence, in addition to trying to obtain maximum acceptance, it is particularly important to understand the effect of any asymmetries in the acceptance which may arise as a result of the real detector efficiencies not being perfectly symmetric or of the beam crossing not being perfectly centred.

#### 3.3.5.3 Likelihood function and fitting procedure

Since a Z′ can be discovered with a small number of events (Section 3.3.4), and since the search for anomalous $A_{\rm FB}$ in the highest mass continuum Drell-Yan events at any given luminosity will use a restricted sample of events, we consider an unbinned likelihood fit. The procedure and results with statistical errors only are described in Ref. [110]. The results of numerous fits can be summarised simply with a nominal statistical uncertainty in $A_{\rm FB}$ of 0.09 in a fit with 400 events for 1 TeV/c$^2$ Z′ samples, and of 0.08 with 400 events for 3 TeV/c$^2$ samples. Ref. [110] also reviews an appropriate hypothesis-testing methodology for distinguishing between Z′ models.

### 3.3.6 Discriminating between different spin hypotheses

In order to distinguish the spins of a spin-1 Z′ bosons and a spin-2 gravitons in a dilepton decay mode, Ref. [114] considers an unbinned likelihood ratio statistic incorporating the angles of the decay products. The statistical interpretation of this statistic is discussed in detail in Ref. [115], also considering the possibility of spin 0.

To leading order, the sub-diagram for Z′ formation is quark-anti-quark ($q\bar{q}$) annihilation, while for a graviton there exist both $q\bar{q}$ annihilation and gluon-gluon ($gg$) fusion. One defines

$\theta^*$ as the angle in the dilepton centre-of-mass reference frame between the negative lepton $\ell^-$ and the incident quark or gluon. In this section we consider only the parity-conserving terms; inference from these terms can be combined with that of the parity-violating terms giving rise to $A_{\mathrm{FB}}$.

For light lepton decay products, the angular probability density functions in the absence of interference are in Table 3.10. These are determined from angular momentum considerations and do not depend on the couplings. For the spin-2 graviton, only the relative fractions of $q\bar{q}$ annihilation, gluon fusion, and background (predominantly from the Drell-Yan continuum) events are needed to arrive at a parameter-free form for the expected distribution. (For spin 1, the resonance and the Drell-Yan background have the same form.)

Table 3.10: Angular distributions for the decay products of spin-1 and spin-2 resonances, considering only even terms in $\cos\theta^*$.

| Channel | $d$-functions | Normalised density for $\cos\theta^*$ |
|---|---|---|
| $q\bar{q} \to \mathrm{G}^* \to f\bar{f}$ | $\left\|d^2_{1,1}\right\|^2 + \left\|d^2_{1,-1}\right\|^2$ | $P_q = \frac{5}{8}\left(1 - 3\cos^2\theta^* + 4\cos^4\theta^*\right)$ |
| $gg \to \mathrm{G}^* \to f\bar{f}$ | $\left\|d^2_{2,1}\right\|^2 + \left\|d^2_{2,-1}\right\|^2$ | $P_g = \frac{5}{8}\left(1 - \cos^4\theta^*\right)$ |
| $q\bar{q} \to \gamma^*/\mathrm{Z}^0/\mathrm{Z}' \to f\bar{f}$ | $\left\|d^1_{1,1}\right\|^2 + \left\|d^1_{1,-1}\right\|^2$ | $P_1 = \frac{3}{8}\left(1 + \cos^2\theta^*\right)$ |

The fractions of generated events arising from these processes are denoted by $\epsilon_q$, $\epsilon_g$, and $\epsilon_1$, respectively, with $\epsilon_q + \epsilon_g + \epsilon_1 = 1$. Then the form of the probability density $P(\cos\theta^*)$ is

$$P(\cos\theta^*) = \epsilon_q P_q + \epsilon_g P_g + \epsilon_1 P_1. \tag{3.24}$$

As in the $A_{\mathrm{FB}}$ measurements, we let $\theta^*_{\mathrm{CS}}$ denote the polar angle of the $\ell^-$ in the Collins-Soper frame. Experimentally one will obtain a set of events with $\theta^*_{\mathrm{CS}}$ measured along with other quantities such as dilepton transverse momentum $p_{\mathrm{T}}^{\mathrm{dil}}$ and rapidity $y^{\mathrm{dil}}$. From these, one can construct the probability density $P_{\mathrm{acc}}(\cos\theta^*_{\mathrm{CS}})$ for events accepted (observed) in an experiment for each hypothesis $H_i$, where $i$ labels the model such as Z′ or G$^*$. In this study, we consider only the angular information and integrate over $p_{\mathrm{T}}^{\mathrm{dil}}$, $y^{\mathrm{dil}}$, and any other relevant quantities; if one has confidence that these quantities are well described by the event generators, more variables can be added to $P_{\mathrm{acc}}$. Since we do not add this information, $P_{\mathrm{acc}}$ for accepted events approximately factorises:

$$P_{\mathrm{acc}}(\cos\theta^*_{\mathrm{CS}}|H_i) = P(\cos\theta^*_{\mathrm{CS}}|H_i)\,\overline{\Omega}(\cos\theta^*_{\mathrm{CS}}), \tag{3.25}$$

where $P(\cos\theta^*_{\mathrm{CS}}|H_i)$ is from Eq. (3.24) with the $\epsilon_j$ set appropriately for the model considered (e.g. for the spin-1 hypothesis, we set $\epsilon_1 = 1$ and $\epsilon_q = \epsilon_g = 0$), and $\overline{\Omega}$ is the acceptance averaged over $p_{\mathrm{T}}$, $y$, etc.

Eq. (3.25) has no free parameters if the fractions $\epsilon_q$, $\epsilon_g$, and $\epsilon_1$ are considered to be fixed. For each observed event, one evaluates $P_{\mathrm{acc}}(\cos\theta^*_{\mathrm{CS}}|H_i)$ at the observed $\cos\theta^*_{\mathrm{CS}}$ to obtain the *likelihood* $\mathcal{L}(H_i)$ of that event under the given hypothesis. The combined likelihood of the data set under a hypothesis is then the product of the events' likelihoods; henceforth in this paper, $\mathcal{L}(H_i)$ refers to this product unless otherwise stated. As Ref. [115] discusses, the absence of free parameters means that the Neyman-Pearson hypothesis testing for *simple* hypothesis testing is applicable.

For testing a simple null hypothesis $H_A$ of one spin against another simple alternative spin hypothesis $H_B$, we use the likelihood ratio $\lambda = \mathcal{L}(H_A)/\mathcal{L}(H_B)$, with critical region again chosen such that $\alpha = \beta$. For investigating and summarising which values of $\lambda^{\rm cut}$ correspond to which values of $\alpha$ and $\beta$, the quantity $-2\ln\lambda = 2\ln\mathcal{L}(H_B) - 2\ln\mathcal{L}(H_A)$ is particularly useful. For simple hypotheses $H_A$ and $H_B$, the central limit theorem implies that $-2\ln\lambda$ tends to a Gaussian.

#### 3.3.6.1 Testing spin 1 versus spin 2

A detailed discussion of the intermediate steps in applying the above method for discriminating spin 1 from spin 2 is in Ref. [115], using large samples of Z′ and $\mathrm{G}^*$ events (from the Randall-Sundrum (RS) model [93]) generated with HERWIG. (Generator-level results using PYTHIA are completely compatible.) The ratio $\lambda$ of the likelihoods of the hypotheses is calculated for each event, assigning spin 1 as the null hypothesis $H_A$ and spin 2 as the alternative hypothesis $H_B$. In taking the ratio, the average acceptance cancels to good approximation and one essentially recovers the ratios of the angular forms. Histograms of $-2\ln\lambda$ for these events are highly asymmetric and strongly peaked at one side [115]. In view of the asymmetries in the underlying event histograms, the convergence of the sums of $-2\ln\lambda$ values for $N$ selected events toward Gaussians is quite striking. The means and rms deviations of the sums are in excellent agreement with the means and rms deviations of the respective event histograms scaled by $N$ and $\sqrt{N}$, respectively, as expected from the central limit theorem.

The statistical technique of Ref. [115] has been applied to fully-reconstructed Z′ and $\mathrm{G}^*$ events [116]. Details of simulation, trigger and reconstruction are described in Sections 3.3.2, 3.3.3 and 14.3.1. From ensembles of pseudo-experiments, we determine the number $N$ of events per experiment corresponding to various values of $\alpha = \beta$, expressed in equivalent number of Gaussian standard deviations "$\sigma$" for *one*-tailed tests, e.g., for $\alpha = 0.159$ we report $\alpha = 1\sigma$, and so on. The values of $\alpha$ so obtained scale as expected as $\sqrt{N}$.

Table 3.11 contains, for different studied masses and values of the Randall-Sundrum ratio $c = k/\bar{M}_{\rm Pl}$, the integrated luminosity needed for a $2\sigma$ significance, and the corresponding numbers of signal and background events. All numbers are for the "long term" misalignment scenario; the cross section for Z′ production is assumed to be equal to that of $\mathrm{G}^*$ with the given $c$ value. Of course, because the production cross section falls rather steeply with mass, the integrated luminosity needed for spin discrimination increases with mass. For RS gravitons, the production cross section scales as $c^2$; therefore, the integrated luminosity required for spin discrimination quickly increases as $c$ gets smaller, and so does the number of signal events, because of a larger background contamination. The region in the plane of $M_{\mathrm{G}^*}$–$c$ in which Randall-Sundrum $\mathrm{G}^*$ can be distinguished from Z′ with $2\sigma$ significance if one treats two spin hypotheses symmetrically is shown in Figure 3.22 for a few representative values of the integrated luminosity.

Alternatives to the $\alpha = \beta$ criterion, in particular tests in which $\alpha$ is minimised for one hypothesis at the cost of increase in $\beta$, are discussed in Ref. [115].

#### 3.3.6.2 Discrimination from spin 0

While the motivation of discriminating Z′ from $\mathrm{G}^*$ has focused studies on discriminating spin 1 from spin 2, another possibility to be considered is spin 0 resonance (which is uniform in $\cos\theta^*$). For accepted spin-0 events, the probability density for $\cos\theta^*_{\rm CS}$ is somewhat in between the mostly concave-upward function for spin 1 and the predominantly concave-

Table 3.11: Integrated luminosity and numbers of signal and background events $N_s$ and $N_b$ required to discriminate spin-1 and spin-2 hypotheses with $\alpha = \beta$ corresponding to $2\sigma$ (one-tailed). The first column indicates the mass of the resonance; the second column shows the values of the RS ratio $c = k/\bar{M}_{\rm Pl}$; the third column specifies the integrated luminosity needed for $2\sigma$ discrimination; the last two columns show the corresponding numbers of signal and background events.

| $\sqrt{s}$, TeV | $c$ | $\int \mathcal{L}dt$, fb$^{-1}$ | $N_s$ | $N_b$ |
|---|---|---|---|---|
| 1.0 | 0.01 | 50 | 200 | 87 |
| 1.0 | 0.02 | 10 | 146 | 16 |
| 1.5 | 0.02 | 90 | 174 | 41 |
| 3.0 | 0.05 | 1200 | 154 | 22 |
| 3.0 | 0.10 | 290 | 148 | 6 |

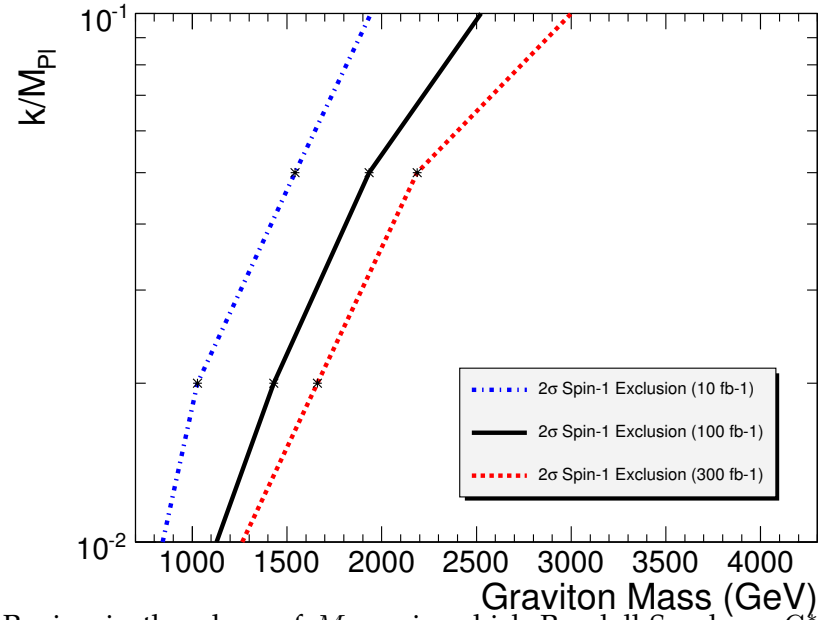


Figure 3.22: Region in the plane of $M_{G^*}$–$c$ in which Randall-Sundrum $G^*$ can be distinguished from Z′ having an equal cross section with $2\sigma$ significance if one treats two spin hypotheses symmetrically, for a few representative values of the integrated luminosity. The region which can be probed lies to the left of the lines.

downward function for spin 2.

As discussed in Ref. [115], discriminating either spin 1 or spin 2 from spin 0 requires significantly more events than discriminating spin 2 from spin 1.